Bulletin of the Seismological Society of America
2023, Volume 113, Issue 4, Pages 1523-1541
https://doi.org/10.1785/0120220213
https://archimer.ifremer.fr/doc/00836/94784/

Hydroacoustic Study of a Seismic Swarm in 2016–2017 near the Melville Transform Fault on the Southwest Indian Ridge

Vijay Ingale Vaibhav [1, *], Bazin Sara [1], Olive Jean-Arthur [2], Briais Anne [1], Royer Jean-Yves [1]

[1] Lab Geo-Ocean, University of Brest, CNRS, Ifremer, UMR6538, F-29280, Plouzané, France
[2] Laboratoire de Géologie, CNRS—École Normale Supérieure, PSL University, Paris, France

* Corresponding author : Vaibhav Vijay Ingale, email address : vaibhavvijay.ingale@univ-brest.fr

Abstract :

Hydroacoustic monitoring has become particularly efficient for studying the low-magnitude seismicity occurring at mid-ocean ridges. In 2016–2017, a seismic swarm occurred near the Melville transform fault of the ultraslow-spreading Southwest Indian Ridge in the Indian Ocean. It comprised 258 events in the land-based International Seismological Centre catalog, extending from June 2016 to March 2017. We examined this seismicity using hydroacoustic records from three to nine hydrophones moored in the southern Indian Ocean from the Hydroacoustic Observatory of Seismicity and Biodiversity in the Indian Ocean (OHASISBIO) temporary network and the International Monitoring System of the Comprehensive Nuclear-Test-Ban Treaty Organization. We detected 27,624 hydroacoustic events spanning 298 days (1 June 2016–25 March 2017) with lower localization and origin time errors. These include several energetic, short-duration impulsive events, which we interpret as due to lava–water interactions on the seafloor. The spatio-temporal distribution of all the detected events does not show clear tectonic mainshock–aftershock sequences and suggests a magmatic origin of the swarm with bursts of seismicity likely caused by dike emplacements.

Key points:

1. This hydroacoustic study focuses on one of the strongest seismic swarms along the Southwest Indian Ridge
2. Short, energetic impulsive events are attributed to hot lava and seawater interaction on the seafloor
3. The seismicity distribution suggests magmatic origin of the swarm, caused by dike emplacements

Introduction

Along mid-ocean ridges (MORs) or divergent boundaries separating tectonic plates, the oceanic lithosphere is created by a complex interplay of magmatic and tectonic processes, which result in numerous earthquakes that have been investigated since the 1970s (e.g., Sykes, 1970; Bergman and Solomon, 1990; Tolstoy et al., 2001; Rundquist and Sobolev, 2002; Tolstoy and Bohnenstiehl, 2006; Schlindwein et al., 2015; Yu et al., 2018). The associated low-level seismicity is generally lacking in records from land-based seismic networks due to the remoteness of MORs and the rapid attenuation of seismic waves in the solid Earth (Fox et al., 2001; Korger and Schlindwein, 2012). Since the late 1980s, local studies using ocean-bottom seismometers (OBS; e.g., Toomey et al., 1985; Wolfe et al., 1995; Tolstoy et al., 2008; Sahoo et al., 2021) and regional studies using autonomous underwater hydrophones (e.g., Fox et al., 1995; Smith et al., 2003; Bohnenstiehl et al., 2008; Royer et al., 2015) have greatly contributed to a comprehensive understanding of MOR seismicity. This is possible because low-frequency hydroacoustic T-waves from seismic events propagate over long distances with little attenuation within the ocean's low-velocity waveguide, known as the Sound Fixing and Ranging (SOFAR) channel (Tolstoy and Ewing, 1950; Weston and Rowlands, 1979; Fox and Squire, 1994). Earthquakes excite T-waves in the water column through the conversion of seismic waves into acoustic waves at the seafloor (Fox et al., 1995, 2001; Dziak et al., 2012; Jamet et al., 2013). T-wave detection studies provide insights into magmato-tectonic processes and transform fault dynamics over large sections of MORs (Dziak et al., 1997; Bohnenstiehl et al., 2002; Smith et al., 2002; Bohnenstiehl et al., 2003; McGuire et al., 2005; Olive and Escartín, 2016; Giusti et al., 2018; Parnell-Turner et al., 2022). This is the reason why the OHASISBIO (Hydroacoustic Observatory of Seismicity and Biodiversity in the Indian Ocean) network of hydrophones was set up in

2010 to simultaneously monitor the three Indian Ocean ridges with contrasting spreading rates (Royer, 2009). This long-term network has captured 15 swarms since 2010 (e.g., Tsang-Hin-Sun et al., 2016; Ingale et al., 2021), particularly along the Southwest Indian Ridge (SWIR). This paper focuses on the strongest, longest and most recent swarm on the SWIR.

The ultraslow-spreading SWIR, with a full spreading rate of ~14 mm/a (Cannat et al., 1999; Chu and Gordon, 1999), is a major spreading ridge that has separated Africa from Antarctica for over 100 Ma (Patriat et al., 1997). It extends from the Bouvet Triple Junction (BTJ) in the southern Atlantic Ocean to the Rodrigues Triple Junction (RTJ) in the Indian Ocean (Figure 1a; Royer et al., 1988, 1989). Its western end (BTJ) is older than its eastern end (RTJ) due to the lengthening and eastward propagation of the ridge axis at the RTJ (Patriat and Ségoufin, 1988). It is characterized by several large-offset transform faults that divide the ridge into spreading segments of varying lengths (Mendel et al., 1997) with several magmatic and amagmatic ridge segments (Dick et al., 2003) marked by a deep axial valley bounded by ~3 km-high ridges (Sauter and Cannat, 2010). The cyclic nature of volcanic construction and tectonic dismemberment across the SWIR has shaped its rugged morphology (Mendel et al., 2003).

The Melville Transform Fault (TF) offsets the SWIR axis to the north by ~150 km (Parson et al., 1997) and marks a boundary between two sections of the SWIR in terms of offset, segmentation, bathymetry, seafloor structure, crustal thickness, magma supply, mantle temperature and seismicity distribution (Patriat et al., 1997; Baines et al., 2007). West of the Melville TF (60°45'E), the SWIR shows an obliquity of 40° and contains several long-lived transform and non-transform discontinuities (Figure 1a). The section east of the Melville TF and up to RTJ (70°E) has an obliquity of 25° and is continuous with minor discontinuities. Also, segments east of the Melville TF have a less regular pattern of Mantle Bouguer gravity anomalies (MBA), compared with segments west of it (Rommevaux-Jestin et al., 1997). This observation can be explained by a quasi-amagmatic spreading of the SWIR east of the Melville TF, with multiple detachment faults exhuming mantle rocks and scarce volcanic constructions (Sauter et al., 2004). The along-axis depth profile near the Melville TF shows striking variations with bathymetric highs shallower than 3000 m adjacent to axial depth maxima (valley) deeper than 6000 m. Next to this transform fault valley, the obliquity of the ridge axis reaches 40° at 61°25'E. It also shows a spectacular bathymetric high near 61°25'E with peak-to-trough relief reaching 3700 m and a depth gradient of up to 130 m/km (Patriat et al., 1997). East of this bathymetric high, the rift valley is oblique and continuous up to 63°30'E, with depths ranging between 4500 and 5500 m (segment 14 in Cannat et al., 1999). This segment has a large-amplitude MBA low and its gravity signature is broader than the topography, which can be interpreted as thick crust and/or reduced-density crust or mantle (Cannat et al., 1999).

Several seismic studies have been conducted along the SWIR, both east and west of the Melville TF, based on teleseismic observations (e.g., Wiens and Petroy, 1990), hydroacoustic observations (e.g., Tsang-Hin-Sun et al., 2016), or local OBS surveys (e.g., Yu et al., 2018; Schmid et al., 2017). West of the Melville TF, a teleseismic analysis recorded seismicity associated with an along-axis melt flow mechanism (Läderach et al., 2012). East of the Melville TF, several short-term OBS surveys interpreted the observed seismicity as magma movement related to diking episodes (Schlindwein and Schmid, 2016; Meier and Schlindwein, 2018). In the vicinity of the TF (Figure 1b), between June 2016 and March 2017, there was a series of 258 earthquakes reported by the International Seismological Centre (ISC, 2022; triangles in Figure 1b) among which 17 events are reported in the Global Centroid Moment Tensor catalog (GCMT; Ekström

et al., 2012; diamonds in Figure 1b). All of the latter show double-couple normal faulting mechanisms, 16 parallel to the SWIR axis and one parallel to the Melville TF.

To investigate this seismic series from the low-level seismicity lacking in the land-based catalogs due to their detection threshold, we examined hydroacoustic data (T-waves) recorded by autonomous hydrophones moored on either side of the SWIR from the OHASISBIO network (Royer, 2009). The OHASISBIO is a long-term hydroacoustic program for monitoring the seismic activity (e.g., Tsang-Hin-Sun et al., 2016) and the vocal activity of large marine mammals in the southern Indian Ocean (e.g., Samaran et al., 2013; Leroy et al., 2017; Torterotot et al., 2020). The network is maintained during the yearly voyages of R/V *Marion Dufresne* to the French Sub-Antarctic Islands. Along with the OHASISBIO network, we also examined hydroacoustic data from the International Monitoring System (IMS) of the Comprehensive Nuclear-Test-Ban Treaty Organization (CTBTO). This global network is designed to detect sounds generated by underwater explosions (Okal, 2001; Gibbons, 2022). Because the seismicity near the Melville TF is located within the OHASISBIO and CTBTO network, observed hydroacoustic events are likely to have more accurate locations than the events from the ISC catalog. Because the hydrophones are more sensitive to low-magnitude events, we detected 27624 events (circles in Figure 1b), i.e., ~107 times more than in the ISC catalog (258 events). The detailed analysis of this improved and dense catalog of hydroacoustic events helps to understand the nature of seismicity near the Melville TF.

Data and Methods

In comparison with seismic wave propagation in the solid Earth, sound waves propagate in the ocean through a more homogeneous sound-velocity channel. For this reason, hydroacoustic data provide a remarkable improvement in the detection threshold (Fox et al., 1994) as well as location accuracy (Fox et al., 2001; Bohnenstiehl and Tolstoy, 2003) of seismic events, compared to distant land-based seismic networks. In this study, we analyzed data from the OHASISBIO hydrophones (Figure 1a) that are moored in the SOFAR channel axis at depths ranging from 1000 m to 1300 m (Table 1). The hydrophones are located south of La Réunion Island (MAD-W, MAD and MAD-E), north-east and south-west of Amsterdam Island (NE-AMS and SW-AMS), south of the Southeast and Southwest Indian ridges (S-SEIR and S-SWIR), and west of Kerguelen Island (WKER2). All sites had a single hydrophone except the SW-AMS, which had a triad of 3 hydrophones. These hydrophones were all set to record acoustic waves continuously at a rate of 240 Hz on 3-byte-long samples. Both before deployment and after recovery, their high-precision clocks are synchronized with a Global Positioning System clock clock to account for the instrument clock-drift (in the range of 0.002 to 0.100 ppm; Table 1). Among these sites, the hydrophone at MAD was operational from June 2016 to December 2016. In the SW-AMS triad of hydrophones, only SW-AMS3 was operational between June 2016 and November 2016. In January 2017, the SW-AMS triad was replaced by a single hydrophone and the MAD site was no longer operational. However, other sites like MAD-W, MAD-E, NE-AMS and S-SWIR started operating at this time. In the entire duration (June 2016 to March 2017) WKER2 and S-SEIR sites recorded data without any significant intermission.

In the Indian ocean, IMS-CTBTO hydrophones are located ~180 km northwest (H08N) and ~25 km south (H08S) of Diego Garcia Island, ~100 km southwest off Cape Leeuwin, Australia (H01W), and ~30 km north (H04N) of Crozet Island (Figure 1a inset). All these sites comprise a triad of hydrophones also moored in the SOFAR channel and deployed in a triangular configuration with ~2 km spacing between

instruments. They are similarly set to record acoustic waves continuously at a rate of 250 Hz with 24-bit analog-to-digital resolution. For this study, we only used one hydrophone from the H08S (H08S1) and H01W triads (H01W1). We could neither use the H04N triad since it started recording after May 2017 nor the H08N one because it is situated north of the Chagos Bank, which blocked T-waves generated near the Melville TF.

The data from these hydrophones were simultaneously analyzed with the "Seas" software developed at the Pacific Marine Environment Laboratory (PMEL) of the National Oceanic and Atmospheric Administration (Fox et al., 2001) and procesed as described by Royer et al. (2015). Each earthquake was located after manually picking the highest T-wave energy in spectrograms (Figure S1; Schreiner et al., 1995; Slack et al., 1999). If two events originate from the same location at different times (> 40 s), or if two events occur at the same time at different locations, the energy arrivals will be distinct (and "pickable") on all hydrophones due to the spread of the network. Once T-waves were identified on three or more hydrophones, the source location and origin time in UTC were estimated by trial and error using a non-linear least square minimization of the arrival times (Fox et al., 2001). Sound velocities in the ocean were based on the three-dimensional and seasonal Global Digital Environment Model at a resolution of 30 arc-minutes in latitude and longitude (Teague et al., 1990); then the distances and arrival times on each hydrophone were calculated and averaged along great circles joining the sources to each of the receivers. The errors in latitude, longitude and origin time were estimated from the covariance matrix of this least square minimization, weighted by the mean square of the residuals.

Hydroacoustic events are characterized by the acoustic magnitude or Source Level (SL) of the T-waves. The SLs are derived from the Received Levels (RL) at each hydrophone and corrected for the transmission loss (TL) between the event and the hydrophone locations. The TL accounts for the cylindrical sound-spreading loss between the event location and the hydrophone, as well as the spherical sound-spreading loss in the water column between the seafloor acoustic radiator and the sound channel axis (e.g., Jensen et al., 1994). The RL, expressed in decibels with respect to 1 micro-Pascal at 1 meter (dB re µPa at 1 m, hereinafter dB), is based on the average power spectral density in a 10s time-window centered on the peak of energy in the acoustic signal. The RLs are calculated in the 5-60 Hz frequency range, which is optimal for T-wave spectra. This simple RL calculation is performed as the arrival times are picked, and is thus convenient when processing large amounts of data. Furthermore, it is also consistent with previous studies by the PMEL or our group. Methods taking into account scattering effects due to bathymetry or based on T- phase envelopes are perhaps more physically realistic, but require more post-processing and thus are limited to the analysis of small datasets (Yang and Forsyth, 2003).

All the OHASISBIO hydrophones are equipped with HTI-90U sensors with similar sensitivities near -163.5 dB, provided by the manufacturer, except at site SW-AMS3, equipped with an HTI-04ULF sensor with a sensitivity of -168.6 dB (Table 1). Due to this difference in sensitivity, the RL on SW-AMS3 hydrophone differed greatly from that at all other sites. As an example, for some representative events, the median RL was 98.5 ± 2.8 dB on MAD, 102.4 ± 2.6 dB on S-SEIR, 108.3 ± 2.9 dB on WKER2, whereas it was 131.2 ± 3.9 dB on SW-AMS3 (Figure S2a). After correcting these RLs for the transmission loss, SLs for these events detected using all 4 stations was 230.9 ± 3.9 dB, whereas it was 211.1 ± 1.9 dB for the same events picked without SW-AMS3, resulting in a difference of 19.8 dB (Figure S2b). So, instead of recomputing all the SLs to account for this sensitivity discrepancy, we simply reduced them by 19.8 dB

when the events were picked using SW-AMS3 until November 28, 2016 (when it failed). Since the same sensor was redeployed at SW-AMS in January 2017, the SLs were also corrected by the same amount (19.8 dB) when SW-AMS was used in the triangulation.

The hydroacoustic catalog (hereinafter OHA) was built in a two-iteration process. In the first iteration, we manually picked T-wave arrivals in a window size of 30 minutes and constructed a catalog with the following information: the event ID; the number and names of hydrophones used to locate the event; its latitude, longitude and SL; the 1σ uncertainties in latitude, longitude, origin time and SL. In the second iteration, this information was used to zoom-in on the events in a 10-minute time-window to manually re-pick the arrival times and relocate the hydroacoustic events with a higher precision. This step improved the locations and times of the OHA events by reducing the errors in latitude, longitude and origin time by ~8-fold. In the first iteration, the median errors were 2.88 km in latitude, 2.90 km in longitude and 0.90 s in origin time (Figure S3a); in the second iteration, the error improved to 0.38 km, 0.38 km and 0.11 s, respectively (Figure S3b). These errors are calculated only for events recorded by at least four hydrophones. Out of a total of 27624 detected events, only 2095 events (7.6 %) were located using three hydrophones (between November 28, 2016 and January 06, 2017) and the remaining 25529 events were located using four or more hydrophones.

The detection threshold of the hydrophone network is defined by the SL of completeness (SL_C) which is derived from the frequency-size distribution of the acoustic events (Bohnenstiehl et al., 2002). It can be compared to the magnitude of completeness of seismic events from land-based catalogs. This is based on the assumption that acoustic events follow Gutenberg-Richter's law (Gutenberg and Richter, 1954), where SLs would be proportional to the logarithm of the cumulative number of events:

$$\log N = a - b\,SL \qquad (1)$$

where N is the cumulative number of events with a source-level greater or equal to SL and constants a and b are the intercept and the slope of the line fitting the distribution of events. For the OHA catalog, the SL_C is 206.6 dB, coinciding with the peak of the normal distribution of SL. The roll-off point of this Gutenberg-Richter's fitting (equation 1) was 14013 for the OHA catalog (Figure 2a-b). The number of ISC events (258) related to this swarm would be too small for a meaningful comparison, furthermore biased towards high magnitudes. We thus considered all ISC events located along the SWIR (i.e., in a similar tectonic context of an ultra-slow spreading ridge) for years 2010 to 2020. The geographical distribution of these events is shown in Figure S4. Still, this collection only amounts to 1933 ISC events vs. 27624 OHA events. The magnitude (*mb*) of completeness of the 1933 ISC catalog events is $M_{C(ISC)}$ = 4.1 *mb* and the event distribution still remains biased towards high magnitudes. The equivalent magnitude of completeness for the OHA catalog $M_{C(OHA)}$ = 3.3 *mb* was estimated by extrapolating the frequency-size distribution with a b-value = 2.98 from the ISC events up to the number of events defining SL_C (Figure 2c). This magnitude of completeness is 0.8 *mb* better than $M_{C(ISC)}$ and demonstrates that hydrophone arrays provide more complete information about the seismicity along remote mid-oceanic ridges than land-based catalogs. The total number of events detected by the OHASISBIO and CTBTO networks over 10 months at a single location (June 2016 – March 2017) is ~14 times bigger than that detected by land-based networks over 10 years along the whole SWIR (2010-2020). Similar approaches for comparing M_C and SL_C have been used for hydroacoustic events detected along MORs (Bohnenstiehl et al., 2002; Olive and Escartín, 2016; Tsang-Hin-Sun et al., 2016). The b-value = 2.98 for the ISC catalog means that there is likely

a deficit of large events ($M_{C(ISC)}$ > 4.1) relative to small ones. This deficit suggests that a b = 0.47 slope for the SL is representative of a volcanic context.

Fitting the two Gutenberg-Richter laws for OHA and ISC catalogs would yield a relationship of SL = 6.25 *mb* + 186.00, or conversely *mb* = 0.16 SL – 29.76, similar to that proposed, for instance, along the North Mid-Atlantic Ridge, where SL = 7.98 *mb* + 193.58 (Pan and Dziewonski, (2005). However, such relations generally fail to explain the scatter of *mb* vs. SL distribution of the events commonly identified in both hydroacoustic and teleseismic catalogs.

Results

Based on the ISC catalog, the seismic activity started with an event of 4.2 *mb* on June 9, 2016 at 21:50 UTC (SL = 211.7 dB) followed by 257 events until March 25, 2017 with magnitudes ranging between 3.2 *mb* (December 14, 2016 at 11:22) and 5.7 *mb* (January 29, 2017 at 16:42). Such events have SLs between 201.5 and 222.5 dB after the RL corrections. During this period, 17 GCMT catalog events were also reported with magnitudes ranging between Mw = 4.8 (August 5, 2016 at 10:43 and August 6, 2016 at 01:11) and Mw = 5.5 (September 16, 2016 at 18:38) within the same SL range (Figure 3a). We examined the available hydroacoustic records from June 1, 2016 to March 25, 2017 (298 days), yielding a total of 27624 events showing a 107-fold increase in event count and with SLs ranging from 185.8 dB to 227.9 dB. The events between November 28, 2016 and January 20, 2017 were picked on all hydrophones except at the SW-AMS site; hence their SL is not corrected. In these detections, 627 events showed anomalously high SL between January 9 and January 20, 2017. Their median SL was 216.2 ± 6.0 dB, which was higher by 9.6 dB than the median SL of all hydroacoustic events. Here, events were localized using S-SWIR, WKER2, S-SEIR and MAD-W stations of the OHASISBIO network. Such high SL is mainly due to relatively high RL of 118.8 ± 7.3 dB at the S-SWIR site, compared with RL of 106.0 ± 2.3 dB at WKER2, 101.1 ± 3.4 dB at S-SEIR and 100.9 ± 3.4 dB at MAD-W (Figure S5). The large dispersion in RL recorded by station S-SWIR is probably caused by a high noise-level in the ocean (storm induced) or to strumming noise since the mooring is located near the front of the deep circumpolar Antarctic current (see Orsi et al., 1995; Rintoul et al., 2001). Data from the WKER2 mooring does not display such a noise level in the 0-20 Hz bandwidth (Figure S6) and is less prone to strumming as it is located south of the main circumpolar current track.

Several peculiar events, clustered on the slopes of bathymetric highs, east of the Melville TF at 61°25'E (Figure 4), are energetic up to 50-60 Hz and of short duration (~10-15s) compared with ~200s T-wave duration for large earthquakes (such as those reported in the ISC catalog). We have detected 118 such events with SLs ranging between 199.4 and 225.1 dB. These signals were only detected at the nearest (MAD at 621 km) as well at the farthest sites (WKER at 1858 km) of the OHASISBIO network, however not by the CTBTO network, probably due to its remoteness from the Melville TF. Hereinafter, we call them impulsive events and will discuss them in the section "Short and energetic impulsive events".

The seismic activity rate was very mild between June 1 and June 8, 2016 with only 73 events and an average of 9 events per day (solid curve in Figure 3b). On June 9, 2016, the seismic activity intensified with 143 events per day (E/D). We detected 2637 events between June 9 and June 30, 2016, ranging between 1 event and 263 E/D. The activity rate increased on June 18 and then on June 30, coinciding with the occurrence of a strong normal faulting GCMT event (June 30 at 12:20, Mw = 5.1, SL = 213.7 dB). In July, there were 4248 events with a frequency of 47 to 244 E/D. The time clustering of strong ISC and

impulsive events coincided with bursts of seismic activity during this period. At the end of July, there were no strong events and lesser hydroacoustic activity. In August, 3638 events were detected with a frequency ranging from 43 to 254 E/D. A normal faulting GCMT event occurred in early August (August 05 at 10:43, Mw = 4.8, SL = 209.4 dB), coincidently with another burst of activity. Two similar events occurred a day later (August 06 at 01:11, Mw = 4.8, SL = 210.6 dB; August 06 at 12:23, Mw = 4.9, SL = 212.4 dB). A temporal cluster of impulsive events also coincided with this burst of activity. Near the end of August, we observed two normal faulting GCMT events (August 25 at 01:02, Mw = 5.0, SL = 216.9 dB and August 27 at 08:59, Mw = 5.0, SL = 218.3 dB) and another burst in seismic activity. Then 4330 events were detected in September, with a minimum of 65 events and a maximum of 272 E/D. In this period, greater seismicity rates coincided with the September 16 at 18:38, Mw = 5.5 event. October 2016 displays the maximum monthly count of events in the entire duration, with a total of 4787 events and rates ranging from 68 to 297 E/D. The maximum number of E/D (297) between June 2016 and March 2017 was reached on October 11, 2016. In November, the cumulative number of events flattened as the seismicity rate decreased with 3076 events and 57 to 220 E/D. A seismic burst on November 10 coincided with a cluster of few impulsive and ISC events. Then 2040 events were detected in December with 13 to 193 E/D.

A new activity burst was observed on December 14, 2016 and another temporal clustering of ISC events coincided with small burst of seismic activity on December 26, 2016. In January 2017, 1240 events ranged between 7 to 101 E/D. A few impulsive and ISC catalog events coincided with another activity burst on January 07, 2017. After this, the seismicity gradually became milder; however, it slightly increased at the end of January 2017 coinciding with the GCMT event (January 29 at 16:42, Mw = 5.4, SL = 222.5 dB) and a dense temporal cluster of impulsive events. In February, 1127 events were detected with a minimum of 11 events and a maximum of 77 E/D. One impulsive event on February 16, 2017 coincided with another seismic activity burst. There was a normal faulting event on February 21 at 11:08 (Mw = 5.0, SL = 214.0 dB), but the activity rate did not increase after its occurrence. In March, there were only 428 events with daily occurrences between 1 and 33 events; the seismic activity gradually ended until March 25, 2017. Overall, despite the observed variations in the seismic rate, the cumulative number of events (dashed curve in Figure 3b) gradually increased until November 10 and became flat after December 14, 2016. Such a long and sawtoothed distribution of events does not resemble a single mainshock-aftershock sequence.

We computed the distance of the median location of all events per day from a reference point (RP) at 29°19’S, 61°04’E (cross in Figure 1b) to observe the average spatial distribution of the events. The coordinate of the RP is the median location of all the events from the OHA catalog and is situated on the downslope of bathymetric highs at 61°25’E, and south of the ridge axis (Figure 1b inset). When it initiated, the seismicity was positioned at ~10 km from the RP with little fluctuations (Figure 3c and Figure 5). After a temporal cluster of ISC and impulsive events between June 09 and 16, the seismicity migrated back-and-forth between the transform valley and bathymetric highs, showing a wider spatial distribution from June 19 to August 03, 2016. At the time of higher activity on August 05 (Figure 3b), the events were focused within a ± 3 km area located ~10 km from the RP. Then the events shifted by ~30 km away from the RP and migrated back-and-forth between the valley and bathymetric highs within a ± 10 km wide area until September 21, 2016. At this time, the events were ~60 km away from the RP and coincided with a short episode of lower seismic activity rate between September and October 2016. Following it, the seismicity

rate was higher and the events focused within an area of ± 10 km, narrowing between the transform valley and bathymetric highs until November 10, 2016. Furthermore, the events densely focused in a narrow ± 2 km area around the RP, until January 20, 2017. Then, events suddenly moved ~30 km away from the RP and formed a narrow band of seismicity (± 10 km) aligned along the ridge axis until February 02, 2017. Afterwards, the events were randomly distributed away from the RP until the seismicity ended.

Discussion

Seismicity and lithospheric strength near Melville TF

With an average temporal distribution of events of ~93 E/D over 298 days, this seismic swarm is the strongest ever reported along the SWIR in terms of duration and total number of events (Schlindwein, 2012; Schmid et al., 2017; Yu et al., 2018). Two other swarms along the SWIR, which occurred in 2018 near Novara TF and near the RTJ, lasted for a shorter duration compared with this one, the former comprising 1109 hydroacoustic events over 13 days (85 E/D) and the latter 4880 events over 33 days (148 E/D; Ingale et al., 2021). The strong seismicity near the Melville TF could result from distinct accretion processes along this section of the SWIR axis, relative to the two other swarms. The Melville TF was established at ~40 Ma, time of the last major change in spreading direction of the SWIR (Patriat et al., 1997). The sub-axial crust and mantle beneath the Melville TF are cooler (Mendel et al., 1997), which is inferred from greater positive anomalies of shear wave velocity in the upper mantle (Forsyth et al., 1987; Debayle and Lévêque, 1997). This cooler mantle beneath the Melville TF results in a stronger lithosphere with a thicker brittle layer, accommodating numerous earthquakes (Schlindwein and Schmid, 2016; Grevemeyer et al., 2019) and an axial valley oblique to spreading. In this Melville TF swarm, large-magnitude events (ISC and GCMT catalogs) are clustered near the axial area, but the low-magnitude events are spread over a wider area and parallel to the ridge axis. The off-axis lithosphere near the Melville TF might therefore be more accommodative to magmato-tectonic seismicity (Rundquist and Sobolev, 2002).

Short and energetic impulsive events

The short duration, high-energy and frequency content suggest that impulsive events (Figure 4) are H-waves (i.e., water borne), meaning that the energy is directly released into the water column and does not travel into the solid crust as do regular T-waves (Bazin et al., 2022). T-waves originating from shallow earthquakes would have a much broader (i.e., dispersed) waveform due to the size of the seismoacoustic conversion area; furthermore, its magnitude should be significant to be detectable as far as 2000 km away (e.g., at WKER2), which is incompatible with a shallow earthquake depth. Additionally, records of earthquakes detected at the MAD site often display P-wave preceding T-wave arrivals by 240 – 280s (Figure S1) which are not observed before impulsive signals. This confirms that the latter events are not due to shallow earthquakes.

Hydroacoustic impulsive events have been observed at other spreading ridges (e.g., Schlindwein and Riedel, 2010; Tan et al., 2016; Caplan-Auerbach et al., 2017; Le Saout et al., 2020) and underwater volcanoes (e.g., Chadwick et al., 2008; Green et al., 2013; Dziak et al., 2015; Crone and Bohnenstiehl, 2019; Tepp et al., 2020; Bazin et al., 2022; Saurel et al., 2022). Tepp and Dziak (2021) presents a review of the different source mechanisms for such events. Among them, the signature of impulsive signals in our study

resembles closely those generated by lava-water interaction when hot lava reaches seafloor, as reported on the East Pacific Rise (Tan et al., 2016) and Juan de Fuca Ridge (Caplan-Auerbach et al., 2017). The cabled array of the Ocean Observatories Initiative recorded thousands of impulsive acoustic signals with SLs in the range of 130 - 190 dB during the Axial seamount eruption on the Juan de Fuca Ridge in 2015, which were interpreted as lava-water interactions and also confirmed by a post-eruption bathymetric survey (Le Saout et al., 2020). During another volcanic eruption off Mayotte Island in 2020-2021, several impulsive events featured SLs, duration and frequency range comparable to ours (Figure S7), and were interpreted as hot lava and seawater interaction based on direct observation of active lava flows (Bazin et al., 2022; Saurel et al., 2022). This result strengthens our interpretation of impulsive events near the Melville TF being associated with hot lava-seawater interactions. However, in the latter studies, the hydrophones were less than 20 km from the Axial seamount (Le Saout et al., 2020) and about 50 km from the volcanic source off Mayotte Island (Bazin et al., 2022). The discrepancy in SL as well as in the number of impulsive events reported in these two studies vs. ours suggest that only the strongest impulsive events (SL > 199 dB; Figure 3a) were captured by the OHASISBIO hydrophones, the closest being 620 km away from their source.

Temporal distribution of events and modified Omori's law

A potential cause for the observed oscillatory pattern (Figure 3b) in the seismicity could be the occurrence of several large tectonic events. Indeed, the decay in seismic activity after a main shock can be characterized by a modified Omori's law (Utsu et al., 1995):

$$n(t) = K(c + t)^{-p}, \qquad (2)$$

where $n(t)$ is the frequency of aftershocks per unit time t. The constants K, c and p are empirically derived. K reflects the productivity of a mainshock and c represents the activity within the earliest part of the sequence. The exponent p shows the aftershock sequence's decay rate and reflects the properties of the fault system (Mogi, 1967) and thermal state of the surrounding lithosphere (Kisslinger and Jones, 1991; Bohnenstiehl et al., 2002; Klein et al., 2006). It ranges from 0.6 to 2.5 with a median of 1.1 based on a compilation of more than 200 aftershock sequences (Utsu et al., 1995). For tectonic seismicity, p-values are generally found in the 0.8-1.2 range (Utsu, 1999; Schmid and Grasso, 2012; Hainzl et al., 2016) and in the range of 0.9 – 1.2 range for various aftershock sequences observed along the oceanic TF (Davis and Frohlich, 1991; Bohnenstiehl et al., 2002).

After a visual inspection of the main changes in the slope of the cumulative distribution of events as well as slope changes following the occurrence of strong ISC or GCMT events in a zoomed temporal window (month-wise), we identified 12 sequences. Each sequence starts with a sudden increase in seismicity rate, noted by a date and asterisk in Figure 3b, followed by a gradual decrease. The duration of all sequences was determined till the number of events per hour reached zero, i.e., the cumulative distribution of events became flat. Three out of these 12 sequences (1, 2 and 9) were not triggered by a large earthquake recorded by ISC or GCMT (Table 2). Out of the remaining 9 sequences, 7 were triggered by normal faulting GCMT events, for which we computed modified Omori's law parameters (equation 2). The sequences 1, 5, 6, 8 and 10 shown in Figures S8, S12, S13, S15 and S16 have p-value < 0.8; hence could not be classified as pure tectonic mainshock-aftershock sequences (Utsu et al., 1995; Schmid and Grasso, 2012). Sequence 2 (Figure S9) has a p-value > 0.8, but it was not triggered by any energetic (high

magnitude) earthquake; hence not classified as a typical tectonic mainshock-aftershock sequence. Although the remaining sequences 3, 4 and 7 shown in Figure S10, S11 and S14 were triggered by Mw > 4.8 events, they were not considered as purely tectonic in nature as they lasted only for a few hours, a duration too short for an aftershock sequence based on the statistical studies of Hainzl et al., (2016). For instance, these authors showed that aftershocks for a Mw > 4.8 tectonic event will last for over 7 days. Sequence 11 was triggered by a *mb* = 3.8 ISC event (Figure S17), after which the number of events kept increasing instead of decreasing as expected for a tectonic sequence. In short, none of the sequences in this seismic swarm appeared purely tectonic in nature. The normal faulting events which triggered changes in the seismic activity rate are thus interpreted as magmato-tectonic earthquakes (McNutt, 1996; Rubin and Gillard, 1998; Müller and Jokat 2000). In short, the sequences triggered by strong normal faulting events, were interpreted as magmato-tectonic in nature, otherwise as magmatic swarms. We discuss the two remaining sequences (9 and 12) in in the section "Geographical distribution of events".

Temporal distribution of events and tidal effects

In this seismic swarm, the temporal occurrence of events displays an oscillatory pattern (Figure 3b) which could be related to either ocean or solid-Earth tide cycles (Sahoo et al., 2021). Several studies have pointed out a tidal triggering of MOR seismicity (Wilcock, 2001; Scholz et al., 2019), with increased seismicity at low tide (Tolstoy et al., 2002; Wilcock, 2009). To test the tidal influence on the seismicity near the Melville TF, we have computed the tidal coefficients for both the ocean and solid-Earth tides using the Global Oceanic Tidal Corrections code (GOTIC2; Matsumoto et al., 2001). It uses Farrell's convolution integral based on an ocean tide model, a land-sea database and a mass loading Green's Function (Farrell, 1972). Near the Melville TF, the ocean tide varies within ± 2 m and the solid-Earth tide within ± 40 cm. To test their influence on the seismicity, we computed the number of hydroacoustic events with respect to the 2nd derivative of both ocean and solid-Earth tide individually. This 2nd derivative measures the rate of change of slope in the tide height; thus, a negative value corresponds to high tide and a positive value to low tide. In our study, 13524 events occurred during high ocean tide and 14100 events during low ocean tide, showing no obvious effect of the ocean tide (Figure S18). Similarly, 13907 and 13717 events occurred during high and low solid-Earth tides, respectively. These results indicate that neither the ocean nor the solid-Earth tidal oscillations clearly govern the seismicity, unlike, for instance, at Axial volcano on Juan de Fuca ridge where the seismicity was predominant during the periods of low tide (Tolstoy et al., 2002; Wilcock et al., 2016).

We also computed the ocean and solid-Earth tidal heights for all 12 sequences and verified whether there was any correlation between the tides and the seismic activity. Only for sequence 9, we could observe that a high seismicity rate coincides with a high ocean tide at the start of the sequence (Table 2). In order to illustrate the range of our observations, we describe two sequences (9 and 12) in the in the "Geographical distribution of events" section that display very distinct characteristics.

Geographical distribution of events

At the onset of seismic activity, the hydroacoustic events had a scattered spatio-temporal distribution (Figure 5), with significant fluctuations in the distance to the RP (Figure 3c). In June and July 2016, events were spread over the transform valley and bathymetric highs on the southern flank of the

axial valley, east of the TF. One explanation could be that their seismic sources took place in a wide area but it is also possible that their sources originated deep within the crust and that the rough seafloor caused hydroacoustic waves to undergo propagation scattering, or a wider seismic to acoustic conversion area (Park et al., 2001; Williams et al., 2006). During the following months, the locations of the hydroacoustic events gradually narrowed down to a stripe along the ridge axis or near bathymetric highs on the flank of axial valley (Figure 3c). Although, individual bursts of seismic activity clearly stand out, no clear lateral migration of the hydroacoustic events could be observed during the entire period. Instead, the observed pattern over time could be explained by a combination of radial focusing as well as upward migration of the seismic sources. One potential geometry that would explain such observations could be diking episodes feeding from magma pooling at the base of the lithosphere. The occurrence of several impulsive events during this initial period (June to October, 2016) could suggest that few of the dikes reach on the seafloor, causing lava-seawater interactions.

On December 14, 2016, the events clustered within a 20 x 20 km area (sequence 9 in Table 2 and Figure 6a) and their rate abruptly increased to ~17 events per hour (from 08:00 to 12:00), followed by a gradual decrease of activity (Figure 6b). We attempted to fit a modified Omori's law (Figure 6c), and obtained a *p*-value of 0.84. Although such *p*-value falls in the range of 0.8-1.2 associated with the tectonic mainshock-aftershock sequences (e.g., Utsu et al., 1995; Utsu, 1999; Schmid and Grasso, 2012), we did not consider this sequence as purely tectonic in origin since it did not feature a triggering energetic earthquake (Figure 6b). Figure 6d shows that the sudden rise in the number of events occurs at oceanic high tide; however, we could not find any causality. The spatial clustering of events combined with a lack of impulsive events argue for a dike emplacement that did not reach the seafloor. This scenario is illustrated by a cartoon (Figure 6e), where all the hydroacoustic events from 14 to 16 December, 2016 are projected along a SW-NE direction, at the apex of potential dikes.

After January 29, 2017, the seismicity spread in another narrow and longer band along the SWIR axis (sequence 12 in Table 2 and Figure 7a). The onset of this series of events coincides with a Mw = 5.4, 12 km deep, normal faulting event on January 29 at 16:42 (SL = 222.5 dB), after which the number of events gradually decreases as well as their SLs (inside dashed rectangle in Figure 7b). Despite these characteristics, this sequence is not considered as purely tectonic mainshock-aftershocks; the Omori's law *p*-value is only 0.54 (Figure 7c), which is much less than 0.8. Furthermore, the sequence only lasted for ~17 hours when it should have lasted at least for ~10 days for a Mw = 5.4 tectonic event (Hainzl et al., 2016). Hence, this sequence is likely to have a magmato-tectonic origin (Rubin, 1992; Giusti et al., 2018). Unlike the sequence in December 2016, tidal loading appears uncorrelated with seismicity rates (Figure 7d). We computed the stress change as a result of slip along a normal fault in an elastic half-space (Meade, 2007). From the two focal planes, we selected the fault plane that dips at 46° towards the axial valley (Figure 7e). Assuming the hydroacoustic relocation (SE of the ridge axis) and the depth from the GCMT catalog (12 km), the Mw = 5.4 event imparted horizontal extension onto the shallow crust below the axial valley, which could have triggered or facilitated the propagation of a vertical dike. The narrow band of events that we interpret as a vertical and elongated dike below the axial valley, has the same SW-NE azimuth as the normal fault bounding the axial valley to the south. The presence of impulsive events argues for the development of a volcanic fissure along the ridge axis. Such an oblique orientation with respect to the spreading direction is expected near the transform valley due to a rotation of extensional

stresses. Afterwards, events scattered over a wider area in February-March 2017 as a result of stress-readjustment in the vicinity (Sohn et al., 1998; Dziak et al., 2004; Rivalta et al., 2015). In this last stage, a double-couple event occurred in February 2017 with a focal mechanism parallel to the Melville TF.

Succession of dike emplacements and normal faulting events

Migration of seismic activity and earthquake locations has been observed at both subaerial and submarine MORs and has been attributed to the vertical and/or lateral propagation of a magma-filled dike at the ridge axis (e.g., Dziak *et al.* 1995; Dziak and Fox 1999; Dziak et al., 2004; Bohnenstiehl *et al.* 2004). Several laterally migrating dike intrusions have already been documented on the SWIR: at segment 18 near the Novara TF and at segment 4 near the RTJ (Ingale et al., 2021), and at segments 7 and 8, east of the Melville TF (Schmid et al., 2017). In this study, we do not observe any lateral migration in the seismic activity. We interpret the bursts of seismic activity as diking episodes, as evidenced by the clustering of events near bathymetric highs at 61°25'E in December 2016 and along a narrow band in the axial valley in January 2017. Moreover, the occurrence of impulsive events suggests that magma has erupted on the seafloor, although there is so far no *in situ* evidence for it (in the absence of recent multibeam bathymetry or side-scan sonar surveys). The normal faulting GCMT and other strong earthquakes (ISC catalog) before December 2016 could have changed the stress regime in the sub-axial crust, changing the overpressure on a sub-seafloor magma body and triggering the emplacement of several dikes (Cannat et al., 2003; Baer et al., 2008; Standish and Sims, 2010; Liu and Buck, 2018; Olive and Dublanchet, 2020) and the events after December 2016 likely represented the reactivation of faults in response to stress perturbation caused by the magma eruption (Toda et al., 2002; Shuler and Nettles, 2012). As summarized in Table 2, we propose that these strong tectonic events occur in magmatic swarms, instead of distinct mainshock-aftershock sequences, as described by McNutt (1996) in a volcanic context, and have a magmato-tectonic origin as described by Rubin and Gillard (1998). Similar observations of a magmatic swarm comprising several normal faulting events were made on the ultraslow-spreading Gakkel ridge (Müller and Jokat 2000) and later confirmed by *in situ* sonar imaging (Edwards et al., 2001). The combined evidence of seismic activity bursts, absence of clear mainshock-aftershock sequences and occurrence of impulsive events point to a magmatic origin for this long-lasting and intense swarm near the Melville TF.

Conclusions

Due to the remoteness of the Southwest Indian Ridge, most of its seismicity is known from teleseismic records over several decades but limited to magnitudes larger than mb = 4.1. Furthermore, in situ seismicity recordings by ocean bottom seismometers are rare and limited in time. Long-term seismic monitoring with autonomous hydrophone networks bridges this gap by capturing lower magnitude (down to mb = 3.3, this study) and transient events.

Here, we analyzed hydroacoustic T-waves associated with a swarm that occurred in 2016-2017, near the Melville TF, along the SWIR, using data from the OHASISBIO and IMS-CTBTO hydrophone networks. The main findings of this study are:

1. This swarm lasted for 298 days from June 01, 2016 to March 25, 2017 and counted 27624 hydroacoustic events, the strongest swarm reported on the SWIR so far.

2. The detection of events over two iterations reduced the uncertainties in location (latitude and longitude) and origin time by ~eight-fold; these were improved to < 400 m in latitude and longitude and 0.1 s in origin time. Despite short periods of noisy data, the general high detection level allowed to identify twelve bursts of activity within this seismic swarm.
3. Although T-wave catalogs lack information about the source depth, we interpret the gradual clustering of earthquakes and the different bursts of seismic activity as the results of several dike emplacements. In addition, bands of events parallel to the SWIR axis imply the transport of magma along narrow and elongated vertical dikes. Normal faulting events were observed as magmato-tectonic in origin and associated with fault activation as well as a response to stress perturbation.
4. We detected a series of energetic and short duration (10 -15s) impulsive events, up to ~2000 km away from their source. We interpret them as water-borne H-waves associated with hot lava-seawater interactions caused by magma emplacement on the seafloor. However, there is yet no in situ evidence to confirm any recent eruption near the Melville TF, which calls for future near-bottom surveys.
5. The occurrence of impulsive events, the spatio-temporal distribution of the events and the absence of clear tectonic mainshock-aftershock sequences point to the magmatic nature of this swarm.

To understand the spatio-temporal distribution of seismicity and nature of this seismic swarm, T-wave signals were visually examined and manually picked in spectrograms where they are more discernible than in waveforms, particularly for low-magnitude events. Such analytical procedure is cumbersome and its efficiency may differ from one operator to another. As a prospective, designing a processing algorithm based on machine-learning would be a tremendous improvement (Raumer et al., 2023).

Data and Resources: The hydroacoustic catalog presented in this study is available upon request to the senior authors (SB & JYR). The supplementary material provides plots of RLs of representative events, of the improvements in the location and time errors, of the ISC catalog events along the SWIR from 2010 to 2020, of impulsive signal waveforms from this study and off Mayotte Island, of the spatio-temporal distribution with best-fitting modified Omori's law, and of number of hydroacoustic events vs. tidal heights. All figures were drafted with the Generic Mapping Tool (GMT; Wessel and Smith, 1998).

Acknowledgments: The French Polar Institute (IPEV) and the French Oceanographic Fleet funded the ship time for the deployment and recovery of the OHASISBIO network. The National Institute for Earth Sciences and Astronomy (INSU) of Centre National de la Recherche Scientifique (CNRS) provided additional support, and the Regional Council of Brittany (CPER) funded the hydrophone moorings. V.V.I. was supported by a fellowship from the University of Brest and from the Regional Council of Brittany, through the ISblue project, Interdisciplinary graduate school for the blue planet (ANR-17-EURE-0015 under the French government's program "Investissements d'Avenir" for France 2030). The authors wish to thank the captains and crew of R/V Marion Dufresne for the successful deployments and recoveries of the hydrophones of the OHASISBIO experiment. The authors acknowledge anonymous reviewers for their

insightful comments and suggestions to improve the manuscript and discussion about the impulsive events.

Declaration of Competing Interests: The authors declare no competing interests.

Author Contribution: Experiment conception and data acquisition, J.-Y.R.; Analysis and original manuscript, V.V.I.; Manuscript edition, V.V.I., S.B. and J.-Y.R.; Resources, J.-Y.R. and S.B. All the authors have contributed to the data interpretation, manuscript revision, and approved the submitted version.

References

Baer, G., Y. Hamiel, G. Shamir, and R. Nof (2008). Evolution of a magma-driven earthquake swarm and triggering of the nearby Oldoinyo Lengai eruption, as resolved by InSAR, ground observations and elastic modeling, East African Rift, 2007, *Earth. Planet. Sci. Lett.* **272**(1-2), 0–352, doi: 10.1016/j.epsl.2008.04.052.

Baines, A. G., M. J. Cheadle, H. J. B. Dick, A. H. Scheirer, B. E. John, N. J. Kusznir, and T. Matsumoto (2007). Evolution of the Southwest Indian Ridge from 55°45'E to 62°E: Changes in plate-boundary geometry since 26 Ma, *Geochem. Geophys. Geosyst.* **8**, Q06022, doi: 10.1029/2006GC001559.

Bazin S., J.-Y., Royer, F. Dubost, F. Paquet, B. Loubrieu, A. Lavayssière, C. Deplus, N. Feuilet, É. Jacques, E. Rinnert, I. Thinon, E. Lebas, D. Pierre, L. Retailleau, J.-M. Saurel, A. Sukhovich, R. Bonnet and the REVOSIMA group (2022). Initial results from a hydroacoustic network to monitor submarine lava flows near Mayotte Island, *C. R. Geosci.* **1**, 0, doi: 10.5802/crgeos.119.

Bergman, E. A., and S. C. Solomon (1990). Earthquake swarms on the Mid-Atlantic Ridge: Products of magmatism or extensional tectonics? *J. Geophys, Res.* **95**, 4943–4965, doi: 10.1029/JB095iB04p04943.

Bohnenstiehl, D. R., M. Tolstoy, R. P. Dziak, C. G. Fox, and G. Smith (2002). Aftershock sequences in the mid-ocean ridge environment: An analysis using hydroacoustic data, *Tectonophysics* **354**, 49–70, doi: 10.1016/S0040-1951(02)00289-5.

Bohnenstiehl, D. R., and M. Tolstoy (2003). Comparison of teleseismically and hydroacoustically derived earthquake locations along the north-central Mid-Atlantic Ridge and Equatorial East Pacific Rise, *Seism. Res. Lett.* **74**, 791–802, doi: 10.1785/gssrl.74.6.791.

Bohnenstiehl, D. R., M. Tolstoy, M., D. K. Smith, C. G. Fox, and R. P. Dziak (2003). Time-clustering behavior of spreading-center seismicity between 15 and 35 N on the Mid-Atlantic Ridge: Observations from hydroacoustic monitoring, *Phys. Earth Planet. Int.* **138**, 147–161, doi: 10.1016/S0031-9201(03)00113-4.

Bohnenstiehl, D. R., R. P. Dziak, M. Tolstoy, C. G. Fox, and M. Fowler, (2004). Temporal and spatial history of the 1999–2000 Endeavour Segment seismic series, Juan de Fuca Ridge, *Geochem. Geophys. Geosyst.* **5**(9), Q09003, doi: 10.1029/2004GC000735.

Bohnenstiehl, D. R., F. Waldhauser, and M. Tolstoy (2008). Frequency-magnitude distribution of microearthquakes beneath the 9°50'N region of the East Pacific Rise, October 2003 through April 2004, *Geochem. Geophys. Geosyst.* **9**, Q10T03, doi: 10.1029/2008GC002128.

Cannat, M., C. Rommevaux-Jestin, D. Sauter, C. Deplus, and V. Mendel (1999). Formation of the axial relief at the very slow spreading Southwest Indian Ridge (49° to 69°E), *J. Geophys. Res.* **104**, 22825–22843, doi: 10.1029/1999JB900195.

Cannat, M., C. Rommevaux-Jestin, and H. Fujimoto (2003). Melt supply variations to a magma poor ultra slow spreading ridge (Southwest Indian Ridge 61° to 69° E), *Geochem. Geophys. Geosyst.* **4**, 9104, doi: 10.1029/2002GC000480.

Caplan-Auerbach, J., R. P. Dziak, J. Haxel, D. R. Bohnenstiehl, and C. Garcia (2017). Explosive processes during the 2015 eruption of axial seamount, as recorded by seafloor hydrophones, *Geochem. Geophys. Geosyst.* **18**, 1761–1774, doi: 10.1002/2016GC006734.

Chadwick, W. W. Jr., K. V. Cashman, R. W. Embley, H. Matsumoto, R. P. Dziak, C. E. J. de Ronde, T. K. Lau, N. D. Deardorff, S. G. Merle (2008). Direct video and hydrophone observations of submarine explosive eruptions at NW Rota-1 Volcano, Mariana Arc, *J. Geophys. Res.* **113**, B08S10, doi: 10.1029/2007JB005215.

Chu, D., and G. R. Gordon (1999). Evidence for motion between Nubia and Somalia along the Southwest Indian Ridge, *Nature* **398**, 64–67, doi: 10.1038/18014.

Crone, T. J., and D. R. Bohnenstiehl (2019). Acoustic evidence of a long-lived gas-driven submarine volcanic eruption in the Bismarck Sea, *Geophys. J. Int.* **217**(1), 169-178, doi: 10.1093/gji/ggy542.

Davis, D. S., C. Frohlich (1991). Single-link cluster analysis, synthetic earthquake catalogues, and aftershock identification, *Geophys. J. Int.* **104**, 2, 289–306, doi: 10.1111/j.1365-246X.1991.tb02512.x.

Debayle, E., and J.-J. Lévêque (1997). Upper mantle heterogeneities in the Indian Ocean from waveform inversion, *Geophys. Res. Lett.* ***24***, 245–248, doi: 10.1029/96GL03954.

Dick, H. J., J. Lin, and H. Schouten (2003). An ultraslow-spreading class of ocean ridge, *Nature* **426**, 405–412, doi: 10.1038/nature02128.

Dziak, R. P., C. G. Fox, and A. E. Schreiner (1995). The June–July 1993 seismo- acoustic event at CoAxial segment, Juan de Fuca Ridge: evidence for a lateral dike injection, *Geophys. Res. Lett.* **22,** 135–138, doi: 10.1029/94GL01857.

Dziak R. P., C. G. Fox, H. Matsumoto, and A. E. Schreiner (1997). The 1992 Cape Mendocino earthquake sequence: Seismo-Acoustic analysis using fixed hydrophone arrays, *Mar. Geophys. Res.* **19**, 137-162, doi: 10.1023/A:1004256910362.

Dziak R. P., and C. G. Fox (1999). The January 1998 earthquake swarm at axial volcano, Juan de Fuca Ridge: hydroacoustic evidence of a seafloor volcanic activity, *Geophys. Res. Lett.* **26**, 3429-3432, doi: 10.1029/1999GL002332.

Dziak, R. P., D. K. Smith, D. R. Bohnenstiehl, C. G. Fox, D. Desbruyeres, H. Matsumoto, M. Tolstoy, and D. J. Fornari (2004). Evidence of a recent magma dike intrusion at the slow spreading Lucky Strike segment, Mid-Atlantic Ridge, *J. Geophys. Res.* **109,** B12102, doi: 10.1029/2004JB003141.

Dziak, R. P., D. R. Bohnenstiehl, and D. K. Smith (2012). Hydroacoustic monitoring of oceanic spreading centers: Past, present, and future, *Oceanography* **25**, 116–127, doi: 10.5670/oceanog.2012.10.

Dziak, R. P., D. R. Bohnenstiehl, E. T. Baker, H. Matsumoto, J. Caplan-Auerbach, R. W. Embley, S. G. Merle, S. L. Walker, T.-K. Lau, and W. W. Chadwick Jr. (2015). Long-term explosive degassing and debris flow activity at West Mata submarine volcano, *Geophys. Res. Lett.* **42**, 1480–1487, doi: 10.1002/2014GL062603.

Edwards, M. H., G. J. Kurras, M. Tolstoy, D. R. Bohnenstiehl, B. J. Coackley, and J. R. Cochran (2001). Evidence of recent volcanic activity on the ultraslow-spreading Gakkel Ridge, *Nature* **409**, 808–812, doi: 10.1038/35057258.

Ekström, G., M. Nettles, and A. M. Dziewonski (2012). The global CMT project 2004–2010: Centroid-moment tensors for 13,017 earthquakes, *Phys. Earth Planet. Inter* ***200–201***, 1–9, doi: 10.1016/j.pepi.2012.04.002.

Farrell, W. E. (1972). Deformation of the Earth by Surface Loads, *Rev. Geophys. Space Phys.* **10**, 761-797, doi: 10.1029/RG010i003p00761.

Forsyth, D. W., R. L. Ehrenbard, and S. Chapin (1987). Anomalous upper mantle be- neath the Australian-Antarctic discordance, *Earth Planet. Sci. Lett.* **84**, 471–478, doi: 10.1016/0012-821X(87)90011-2.

Fox, C. G., R. P. Dziak, H. Matsumoto, and A. E. Schreiner (1994). Potential for monitoring low-level seismicity on the Juan-de-Fuca ridge using military hydrophone arrays, *Mar. Technol. Soc. J.* **27,** 22-30.

Fox, C., and V. A. Squire (1994). On the oblique reflexion and transmission of ocean waves at shore fast sea ice, *Phil. Trans. R. Soc. Lond. A* **347**, 185–218, doi: 10.1098/rsta.1994.0044.

Fox, C. G., W. E. Radford, R. P. Dziak, T. K. Lau, H. Matsumoto, and A. E. Schreiner (1995). Acoustic detection of a seafloor spreading episode on the Juan de Fuca Ridge using military hydrophone arrays, *Geophys. Res. Lett.* **22**, 131–134, doi: 10.1029/94GL02059.

Fox, C. G., H. Matsumoto, and T. K. A. Lau (2001). Monitoring Pacific Ocean seismicity from an autonomous hydrophone array, *J. Geophys. Res.* **106**, 4183–4206, doi: 10.1029/2000JB900404.

Gibbons, S. J. (2022). The Hydroacoustic Network of the CTBT International Monitoring System: Access and Exploitation, *Journal for Peace and Nuclear Disarmament*, 1-17, doi: 10.1080/25751654.2022.2129948.

Giusti, M., J. Perrot, R. P. Dziak, A. Sukhovich, and M. Maia (2018). The August 2010 earthquake swarm at North FAMOUS–FAMOUS segments, Mid-Atlantic Ridge: Geophysical evidence of dike intrusion, *Geophys. J. Int.* ***215***, 181–195, doi: 10.1093/gji/ggy239.

Green, D. N., L. G. Evers, D. Fee, R. S. Matoza, M. Snellen, P. Smets, and D. Simons (2013). Hydroacoustic, infrasonic and seismic monitoring of the submarine eruptive activity and sub-aerial plume generation at South Sarigan, May 2010, *J. Volcanol. Geotherm. Res.* **257**, 31-43, doi: 10.1016/j.jvolgeores.2013.03.006.

Grevemeyer, I., N. W. Hayman, D. Lange, C. Peirce, C. Papenberg, H. J. A. Van Avendonk, F. Schmid, L. G. de La Peña, and A. Dannowski (2019). Constraining the maximum depth of brittle deformation at slow- and ultraslow-spreading ridges using microseismicity, *Geology* **47** (11), 1069–1073, doi: 10.1130/G46577.1.

Gutenberg, B., and C. F. Richter (1954). *Seismicity of the Earth and Associated Phenomena*, Princeton University Press: Princeton, NJ, USA.

Hainzl, S., A. Christophersen, D. Rhoades, and D. Harte (2016). Statistical estimation of the duration of aftershock sequences, *Geophys. J. Int.* **205**(2), 1180–1189, doi: 10.1093/gji/ggw075.

Ingale V. V., S. Bazin, and J.-Y. Royer (2021). Hydroacoustic observations of two contrasted seismic swarms along the Southwest Indian Ridge in 2018, *Geosciences* **11**(6), 225, doi: 10.3390/geosciences11060225.

ISC International Seismological Center, On-Line Bulletin (2022). Available online: http://www.isc.ac.uk/iscbulletin/search/catalogue/ (last accessed on 10 January 2022).

Jamet, G., C. Guennou, L. Guillon, and J.-Y. Royer (2013). T-wave generation and propagation: a comparison between data and spectral element modeling, *J. Acoust. Soc. Am.* **134**, 3376-3385, doi: 10.1121/1.4818902.

Jensen, F. B., W. A. Kuperman, M. B. Porter, and H. Schmidt (1994). Computational Ocean Acoustic, American Institute of Physics, New York, 14-15.

Kisslinger, C., and L. M. Jones (1991). Properties of aftershock sequences in Southern California, *J. Geophys. Res.* **96**, 11947 – 11958, doi: 10.1029/91JB01200.

Klein, F. W., T. Wright, and J. Nakata (2006). Aftershock decay, productivity, and stress rates in Hawaii: indicators of temperature and stress from magma sources, *J. geophys. Res.* **111**(B7), B07307, doi: 10.1029/2005JB003949.

Korger, E. I. M., and V. Schlindwein (2012). Performance of localization algorithms for teleseismic mid-ocean ridge earthquakes: The 1999 Gakkel Ridge earthquake swarm and its geological interpretation, *Geophys. J. Int.* **188**, 613–625, doi: 10.1111/j.1365-246X.2011.05282.x.

Läderach, C., E. I. M. Korger, V. Schlindwein, C. Müller, and A. Eskstaller (2012). Characteristics of tectonomagmatic earthquake swarms at the Southwest Indian Ridge between 16°E and 25°E, *Geophys. J. Int.* **190**, 429–441, doi: 10.1111/j.1365-246X.2012.05480.x.

Le Saout, M., D. R. Bohnenstiehl, J. B. Paduan, and D. A. Clague (2020). Quantification of eruption dynamics on the north rift at Axial Seamount, Juan de Fuca Ridge, *Geochem. Geophys. Geosyst.* **21**(9), e2020GC009136, doi: 10.1029/2020GC009136.

Leroy, E. C., F. Samaran, J. Bonnel, and J.-Y. Royer (2017). Identification of two potential whale calls in the southern Indian Ocean, and their geographic and seasonal occurrence, *J. Acoust. Soc. Am.* **142**, 1413, doi: 10.1121/1.5001056.

Liu, Z., and W. R. Buck (2018). Magmatic controls on axial relief and faulting at mid-ocean ridges, *Earth Planet. Sci. Lett.* **491**, 226-237, doi: 10.1016/j.epsl.2018.03.045.

Matsumoto, K., T. Sato, T. Takanezawa, and M. Ooe (2001). GOTIC2: A Program for Computation of Oceanic Tidal Loading Effect, *J. Geod. Soc. Jpm.* **47** (1), 243-248, doi: 10.11366/sokuchi1954.47.243.

McNutt, S.R. (1996). Seismic Monitoring and Eruption Forecasting of Volcanoes: A Review of the State-of-the-Art and Case Histories, *Monitoring and Mitigation of Volcano Hazards*. Springer, Berlin, Heidelberg, eds., R. Scarpa, and R. I. Tilling, doi: 10.1007/978-3-642-80087-0_3.

McGuire J. J., M. S. Boettcher, and T. H. Jordan (2005). Foreshock sequences and short-term earthquake predictability on East Pacific Rise transform faults, *Nature* **434**, 457-461, doi: 10.1038/nature03377.

Meade, B. (2007). Algorithms for the calculation of exact displacements, strains, and stresses for triangular dislocation elements in a uniform elastic half space, *Comp. Geosci.* **33**(8), 1064-1075, doi: 10.1016/j.cageo.2006.12.003.

Meier, M., and V. Schlindwein (2018). First in situ seismic record of spreading events at the ultraslow spreading Southwest Indian Ridge, *Geophys. Res. Lett.* **45**, 10360-10368, doi: 10.1029/2018GL079928.

Mendel, V., D. Sauter, L. Parson, and J. R. Vanney (1997). Segmentation and morphotectonic variations along a super slow-spreading center: The Southwest Indian Ridge (57°–70°E), *Mar. Geophys. Res.* **19**, 505–533, doi: 10.1023/A:1004232506333.

Mendel, V., D. Sauter, C. Rommevaux-Jestin, P. Patriat, F. Lefebvre, and L. M. Parson (2003). Magmato-tectonic cyclicity at the ultra-slow spreading Southwest Indian Ridge: Evidence from variations of axial volcanic ridge morphology and abyssal hills pattern, *Geochem. Geophys. Geosyst.* **4**, 9102, doi: 10.1029/2002GC000417.

Mogi, K. (1967). Earthquakes and fractures, *Tectonophysics* **5,** 35-55, doi: 10.1016/0040-1951(67)90043-1.

Müller, C., and W. Jokat (2000). Seismic evidence for volcanic activity discovered in Central Arctic, *Eos Trans. AGU* **81**, 265–269, doi: 10.1029/00EO00186.

Okal, E.A. (2001). T-phase Stations for the International Monitoring System of the Comprehensive Nuclear-Test Ban Treaty: A Global Perspective, *Seismol. Res. Lett.* **72**(2), 186-196, doi: 10.1785/gssrl.72.2.186.

Olive, J.-A., M. D. Behn, E. Mittelstaedt, G. Ito, and B. Z. Klein (2016). The role of elasticity in simulating long-term tectonic extension, *Geophys. J. Int.* **205**, 2, 728-743, doi: 10.1093/gji/ggw044.

Olive, J.-A., and J. Escartín (2016). Dependence of seismic coupling on normal fault style along the Northern Mid-Atlantic Ridge, *Geochem. Geophys. Geosyst.* ***17***, 4128-4152, doi:10.1002/2016GC006460.

Olive, J.-A., and P. Dublanchet (2020). Controls on the magmatic fraction of extension at mid-ocean ridges, *Earth Planet. Sci. Lett.* **549**, 116541, doi: 10.1016/j.epsl.2020.116541.

Orsi, A. H., Whitworth III, T., & Nowlin Jr, W. D. (1995). On the meridional extent and fronts of the Antarctic Circumpolar Current, *Deep Sea Research Part I: Oceanographic Research Papers* ***42*** (5), 641-673, doi: 10.1016/0967-0637(95)00021-W.

Pan, J., and A. M. Dziewonski (2005). Comparison of mid-oceanic earthquake epicentral differences of travel time, centroid locations, and those determined by autonomous underwater hydrophone arrays, *J. Geophys. Res.* **110**, B07302, doi:10.1029/2003JB002785.

Park, M., R. I. Odom, D. J. Soukup (2001). Modal scattering: a key to understanding oceanic T-waves, *Geophys. Res. Lett.* **28** (17), 3401-3404, doi: 10.1029/2001GL013472.

Parnell-Turner, R., D. K. Smith, and R. P. Dziak (2022). Hydroacoustic monitoring of seafloor spreading and transform faulting in the equatorial Atlantic Ocean, *J. Geophys. Res. Solid Earth* **127**, e2022JB024008, doi: 10.1029/2022JB024008.

Parson, L., D. Sauter, V. Mendel, P. Patriat, and R. Searle (1997). Evolution of the Axial Geometry of the Southwest Indian Ocean Ridge between the Melville Fracture Zone and the Indian Ocean Triple Junction – Implications for Segmentation on Very Slow-Spreading Ridges, *Marine Geophysical Researches* **19**, 535–552, doi: 10.1023/A:1004335919592.

Patriat, P., and J. Ségoufin (1988). Reconstruction of the central Indian Ocean, *Tectonophysics* **155**, 211–234, doi: 10.1016/0040-1951(88)90267-3.

Patriat, P., D. Sauter, M. Munschy, and L. M. Parson (1997). A survey of the Southwest Indian Ridge axis between Atlantis II Fracture Zone and the Indian Triple Junction: Regional setting and large scale segmentation, *Mar. Geophys. Res.* **19**, 457–480, doi: 10.1023/A:1004312623534.

Raumer P.-Y., S. Bazin, D. Cazau, J.-Y. Royer, V. V. Ingale, and A. Lavayssiere (2023). Application of machine learning to hydro-acoustic seismic and magmatic events detections, EGU General Assembly 2023, Vienna, Austria, doi: 10.5194/egusphere-egu23-7028.

Rintoul, S. R., C. Hughes, and D. Olbers (2001). The Antractic Circumpolar Current System, *Ocean Circulation and Climate*. New York: Academic Press, eds. G. Siedler, J. Church, and J. Gould, hdl: 10013/epic.13233, ISBN: 0-12-641351-7.

Rivalta, E., B. Taisne, A. P. Bunger, and R. F. Katz (2015). A review of mechanical models of dike propagation: Schools of thought, results and future directions, *Tectonophysics* **638**, 1–42, doi: 10.1016/j.tecto.2014.10.003.

Rommevaux-Jestin, C., C. Deplus, and P. Patriat (1997). Mantle Bouguer Anomaly Along an Ultra Slow-Spreading Ridge: Implications for Accretionary Processes and Comparison with Results from Central Mid-Atlantic Ridge, *Mar. Geophys. Res.* **19**, 481–503, doi: 10.1023/A:1004269003009.

Royer, J.-Y., P. Patriat, H. W. Bergh, and C. R. Scotese (1988). Evolution of the Southwest Indian Ridge from the Late Cretaceous (anomaly 34) to the Middle Eocene (anomaly 20), *Tectonophysics* **155**, 235–260, doi: 10.1016/0040-1951(88)90268-5.

Royer, J.-Y., J. G. Sclater, and D. T. Sandwell (1989). A preliminary tectonic fabric chart of the Indian Ocean, *Proc. Indian Acad. Sci. Earth Planet. Sci.* **98**, 7–24, doi: 10.1007/BF02880373.

Royer, J.-Y. (2009). OHA-SIS-BIO: Hydroacoustic Observatory of the Seismicity and Biodiversity in the Indian Ocean, Available online: https://campagnes.flotteoceanographique.fr/ (accessed on 10 January 2022).

Royer, J.-Y., R. Chateau, R. P. Dziak, and D. R. Bohnenstiehl (2015). Seafloor seismicity, Antarctic ice-sounds, cetacean vocalizations and long-term ambient sound in the Indian Ocean basin, *Geophys. J. Int.* **202**, 748–762, doi: 10.1093/gji/ggv178.

Rubin, A. M. (1992). Dike-induced faulting and graben subsidence in volcanic rift zones, *J. geophys. Res.* **97,** 1839–1858, doi: 10.1029/91JB02170.

Rubin, A. M., and D. Gillard (1998). Dike-induced earthquakes: Theoretical considerations, *J. Geophys. Res.* **103**(B5), 10,017–10,030, doi: 10.1029/97JB03514.

Rundquist, D. V., and P. O. Sobolev (2002). Seismicity of mid-oceanic ridges and its geodynamic implications: A review, *Earth Sci. Rev.* **58**, 143–161, doi: 10.1016/S0012-8252(01)00086-1.

Sahoo, S., B. Senapati, D. Panda, D. K. Tiwari, M. Santosh, B. Kundu (2021). Tidal triggering of micro-seismicity associated with caldera dynamics in the Juan de Fuca ridge, *J. Volcanol. Geotherm. Res* **417**, 107319, doi: 10.1016/j.jvolgeores.2021.107319.

Samaran, F., K. M. Stafford, T. A. Branch, J. Gedamke, J.-Y. Royer, R. P. Dziak, and C. Guinet (2013). Seasonal and geographic variation of southern blue whale subspecies in the Indian Ocean, *PLoS ONE* **8**, e71561, doi: 10.1371/journal.pone.0071561.

Saurel, J.-M., L. Retailleau, C. Deplus, B. Loubrieu, D. Pierre, M. Frangieh, N. Khelifi, R. Bonnet, V. Ferrazzini, S. Bazin, P. Guyavarch, M. Moulin, REVOSIMA Seismology group, REVOSIMA Bathymetry group (2022). Combining hydro-acoustic sources and bathymetric differences to track the vent evolution of the Mayotte eruption, Mozambique Channel, *Front. Earth Sci.* 10:983051, doi:10.3389/feart.2022.983051.

Sauter, D., V. Mendel, C. Rommevaux-Jestin, L. M. Parson, H. Fujimoto, C. Mével, M. Cannat, and K. Tamaki (2004). Focused magmatism versus amagmatic spreading along the ultra-slow spreading Southwest Indian Ridge: Evidence from TOBI side scan sonar imagery, *Geochem. Geophys. Geosyst.* **5** (Q10K09), doi: 10.1029/2004GC000738.

Sauter, D., and M. Cannat (2010). The ultraslow spreading Southwest Indian ridge, In *Diversity of Hydrothermal Systems on Slow Spreading Ocean Ridges*; Geophysical Monograph Series; The American Geophysical Union: Washington, DC, USA **188**, 153–173, doi: 10.1029/2008GM000843.

Schlindwein, V. (2012). Teleseismic earthquake swarms at ultraslow spreading ridges: indicator for dyke intrusions?, *Geophys. J. Int.* **190**(1), 442-456, doi: 10.1111/j.1365-246X.2012.05502.x.

Schlindwein, V. and C. Riedel (2010). Location and source mechanism of sound signals at Gakkel ridge, Arctic Ocean: Submarine Strombolian activity in the 1999–2001 volcanic episode, *Geochem. Geophys. Geosyst.* **11**(1), doi: 10.1029/2009GC002706.

Schlindwein, V., A. Demuth, E. Korger, C. Läderach, and F. Schmid (2015). Seismicity of the Arctic mid-ocean ridge system, *Polar Sci.* **9**, 146–157, doi: 10.1016/j.polar.2014.10.001.

Schlindwein, V., and F. Schmid (2016). Mid-ocean-ridge seismicity reveals extreme types of ocean lithosphere, *Nature* **535**, 276–279, doi: 10.1038/nature18277.

Schmid, A., and J. R. Grasso (2012). Omori law for eruption foreshocks and aftershocks, *J. Geophys. Res. Solid Earth* **117**(B7), doi: 10.1029/2011JB008975.

Schmid, F., V. Schlindwein, I. Koulakov, A. Plötz, and J. R. Scholz (2017). Magma plumbing system and seismicity of an active mid-ocean ridge volcano, *Sci. Rep.* **7**, 42949, doi: 10.1038/srep42949.

Schreiner, A.E., C. G. Fox, and R. P. Dziak (1995). Spectra and magnitudes of T-waves from the 1993 earthquake swarm on the Juan de Fuca Ridge, *Geophys. Res. Lett.* **22**, 139–142, doi: 10.1029/94GL01912.

Scholz, C. H., Y. J. Tan, and F. Albino (2019). The mechanism of tidal triggering of earthquakes at mid-ocean ridges, *Nat Commun.* **10**, 2526, doi: 10.1038/s41467-019-10605-2.

Shuler, A., and M. Nettles (2012). Earthquake source parameters for the 2010 western Gulf of Aden rifting episode, *Geophys. J. Int.* **190,** 111–1122, doi: 10.1111/j.1365-246X.2012.05529.x.

Slack, P. D., C. G. Fox, and R. P. Dziak (1999). P wave detection thresholds, Pn velocity estimates, and T wave location uncertainty from oceanic hydrophones, *J. Geophys. Res.* **104**, 13061–13072, doi: 10.1029/1999JB900112.

Smith D. K., M. Tolstoy, C. G., Fox, D. R. Bohnenstiehl, H. Matsumoto, M. J. Fowler (2002). Hydroacoustic monitoring of seismicity at the slow-spreading Mid-Atlantic Ridge, *Geophys. Res. Lett.* **29** (11), doi: 10.1029/2001GL013912.

Smith, D. K., J. Escartín, M. Cannat, M. Tolstoy, C. G. Fox, D. R. Bohnenstiehl and S. Bazin (2003). Spatial and temporal distribution of seismicity along the northern Mid-Atlantic Ridge (15°–35°N), *J. Geophys. Res.* **108**, 2167, doi: 10.1029/2002JB001964.

Sohn, R. A., J. A. Hildebrand, and S. C. Webb (1998). Postrifting seismicity and a model for the 1993 diking event on the CoAxial segment, Juan de Fuca Ridge, *J. Geophys. Res.* **103**, 9867–9877, doi: 10.1029/98JB00391.

Standish, J. J., K. W. Sims (2010). Young off-axis volcanism along the ultraslow-spreading Southwest Indian Ridge, *Nat. Geosci.* **3**, 286–292, doi: 10.1038/ngeo824.

Sykes, L. R. (1970). Earthquake swarms and sea-floor spreading, *J. Geophys. Res.* **75** (32), 6598– 6611, doi: 10.1029/JB075i032p06598.

Tan, Y. J., M. Tolstoy, F. Waldhauser, and W. Wilcock (2016). Dynamics of a seafloor-spreading episode at the east pacific rise, *Nature* **540**, 261–265, doi: 10.1038/nature20116.

Teague, W. J., M. J. Carron, and J. P. Hogan (1990). A comparison between the Generalized Digital Environment Model and Levitus climatologies, *J. Geophys. Res.* **95**, 7167-7183, doi: 10.1029/JC095iC05p07167.

Tepp, G., and R. P. Dziak (2021). The seismo-acoustics of submarine volcanic eruptions, *J. Geophys. Res. Solid Earth* **126**, e2020JB020912, doi: 10.1029/2020JB020912.

Tepp, G., R. P. Dziak, M. M. Haney, J. J. Lyons, C. Searcy, H. Matsumoto, and J. Haxel (2020). Seismic and hydroacoustic observations of the 2016–17 Bogoslof eruption, *Bull. Volcanol.* **82**, 4, doi: 10.1007/s00445-019-1344-3.

Toda, S., R. S. Stein, and T. Sagiya (2002). Evidence from the AD 2000 Izu islands earthquake swarm that stressing rate governs seismicity, *Nature* **419,** 58–61, doi: 10.1038/nature00997.

Tolstoy, I., and M. Ewing (1950). The T phase of shallow-focus earthquakes, *Bull. Seism. Soc. Am.* **40**, 25–51, doi: 10.1785/BSSA0400010025.

Tolstoy, M., D. R. Bohnenstiehl, M. H. Edwards, and G. J. Kurras (2001). Seismic character of volcanic activity at the ultraslow-spreading Gakkel Ridge, *Geology* **29**, 1139–1142, doi: 10.1130/0091-7613(2001)029<1139:SCOVAA>2.0.CO;2.

Tolstoy, M., F. L. Vernon, O. A. John, and W. K. (2002). Breathing of the seafloor: Tidal correlations of seismicity at Axial volcano, *Geology* **30** (6), 503–506. doi: 10.1130/0091-7613(2002)030<0503:BOTSTC>2.0.CO;2.

Tolstoy, M., and D. R. Bohnenstiehl (2006). Hydroacoustic contributions to understanding the December 26th 2004 great Sumatra-Andaman Earthquake, *Surv. Geophys*. **27**, 633-646, doi: 10.1007/s10712-006-9003-6.

Tolstoy, M., F. Waldhauser, D. R. Bohnenstiehl, R. T. Weekly, and W-Y. Kim (2008). Seismic identification of along-axis hydrothermal flow on the East Pacific Rise, *Nature* **451**, 181–184, doi: 10.1038/nature06424.

Toomey, D. R., S. C. Solomon, G. M. Purdy, and M. H. Murray (1985). Microearthquakes beneath the median valley of the Mid-Atlantic Ridge near 23°N: Hypocenters and focal mechanisms, *J. Geophys. Res.* **90**, 5443–5458, doi: 10.1029/JB090iB07p05443.

Torterotot, M., F. Samaran, K. M. Stafford, and J.-Y. Royer (2020). Distribution of blue whale populations in the Southern Indian Ocean based on a decade of acoustic monitoring, *Deep Sea Res. Part II: Top. Stud. Oceanogr.* **179**, 104874, doi: 10.1016/j.dsr2.2020.104874.

Tsang-Hin-Sun, E., J.-Y. Royer, and J. Perrot (2016). Seismicity and active accretion processes at the ultraslow-spreading Southwest and intermediate-spreading Southeast Indian ridges from hydroacoustic data, *Geophys. J. Int.* **206**, 1232–1245, doi: 10.1093/gji/ggw201.

Utsu, T., Y. Ogata, and R. S. Matsuura (1995). The centenary of the Omori formula for a decay law of aftershock activity, *J. Phys. Earth* **1995**, *43*, 1–33, doi: 10.4294/jpe1952.43.1.

Utsu, T. (1999). Representation and analysis of the earthquake size distribution: A historical review and some new approaches, *Pure Appl. Geophys.* **155**(2–4), 509–535, doi: 10.1007/s000240050276.

Wessel, P., and W. H. Smith (1998). New, improved version of Generic Mapping Tools released, *Eos Trans. Am. Geophys. Union* **79**, 579, doi: 10.1029/98EO00426.

Weston, D. E., and P. B. Rowlands (1979). Guided acoustic waves in the ocean, *Rep. Prog. Phys.* **42**, 347, doi: 10.1088/0034-4885/42/2/003/meta.

Wiens, D. A., and D. E. Petroy (1990). The largest recorded earthquake swarm: Intraplate faulting near the Southwest Indian Ridge, *J. Geophys. Res.* **95**, 4735–4750, doi: 10.1029/JB095iB04p04735.

Wilcock, W. S. (2001). Tidal triggering of microearthquakes on the Juan de Fuca Ridge, *Geophys. Res. Lett.* **28**(20), 3999-4002, doi: 10.1029/2001GL013370.

Wilcock, W. S. (2009). Tidal triggering of earthquakes in the Northeast Pacific Ocean, *Geophys. J. Int.* **179**(2), 1, doi: 10.1111/j.1365-246X.2009.04319.x.

Williams, C. M., R. A. Stephen, and D. K. Smith (2006). Hydroacoustic events located at the intersection of the Atlantis (30°N) and Kane (23°40'N) Transform Faults with the Mid-Atlantic Ridge, *Geochem. Geophys. Geosyst.* **7**, Q06015, doi: 10.1029/2005GC001127.

Wolfe, C. J., G. M. Purdy, D. R. Toomey, and S. C. Solomon (1995). Microearthquake characteristics and crustal velocity structure at 29°N on the Mid-Atlantic Ridge: The architecture of a slow spreading segment, *J. Geophys. Res.* **100**, 24449–24472, doi: 10.1029/95JB02399.

Yang, Y., and D. W. Forsyth (2003). Improving epicentral and magnitude estimation of earthquakes from T phases by considering the excitation function, *Bull. Seismo. Soc. Am.* **93**(5), 2106 - 2122, doi: 10.1785/0120020215.

Yu, Z., J. Li, X. Niu, N. Rawlinson, A. Ruan, W. Wang, H. Hu, X. Wei, J. Zhang, and Y. Liang (2018). Lithospheric structure and tectonic processes constrained by microearthquake activity at the central ultraslow-spreading Southwest Indian Ridge (49.2° to 50.8°E), *J. Geophys. Res. Solid Earth* **123**, 6247–6262, doi: 10.1029/2017JB015367.

Figures :

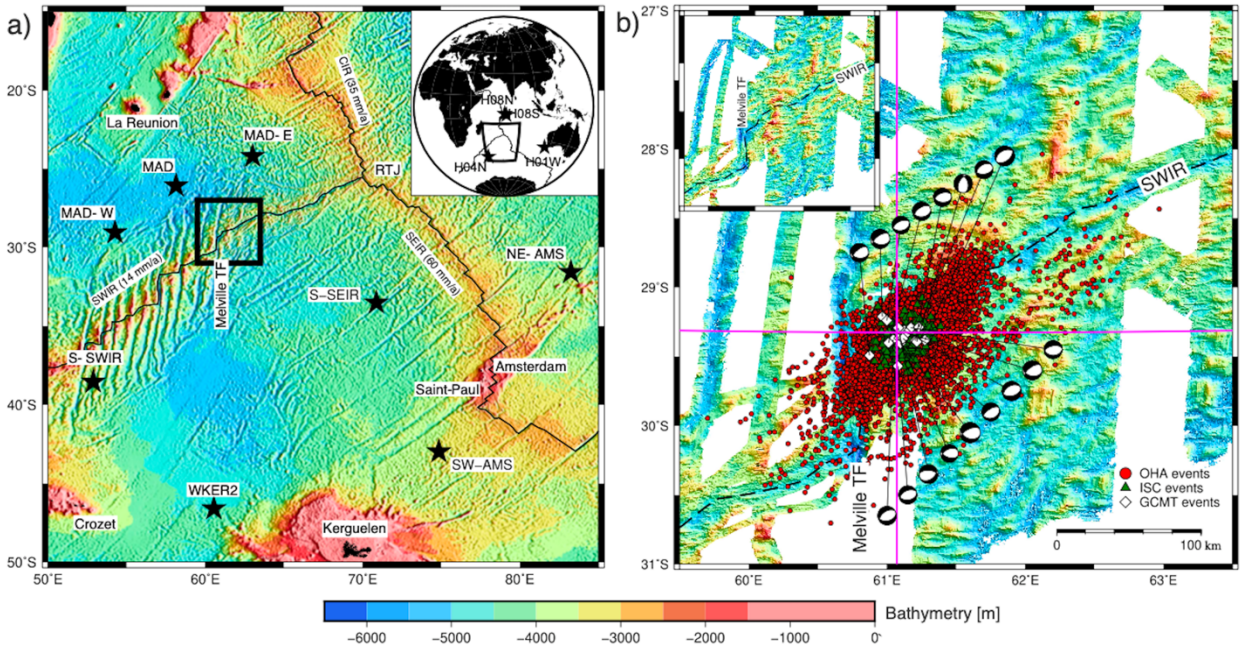

Figure 1: (a) Hydroacoustic Observatory of Seismicity and Biodiversity in the Indian Ocean (OHASISBIO) and International Monitoring System (IMS)– Comprehensive Nuclear-Test-Ban Treaty Organization (CTBTO; inset) net- works of underwater hydrophones (stars). The black lines outline the Southwest Indian ridge (SWIR), Central Indian Ridge (CIR), and Southeast Indian Ridge (SEIR) with their respective spreading rates. (b) The black rectangle shows the study area with the hydroacoustic events detected by the hydrophones (circles) and by the International Seismological Centre (ISC; triangles) and Global Centroid Moment Tensor (Global CMT; diamonds with focal mechanisms) land-based networks. The cross is the median location of all detected events (referred to RP for reference point in the "Results" section). The inset shows the same bathymetric map without events.

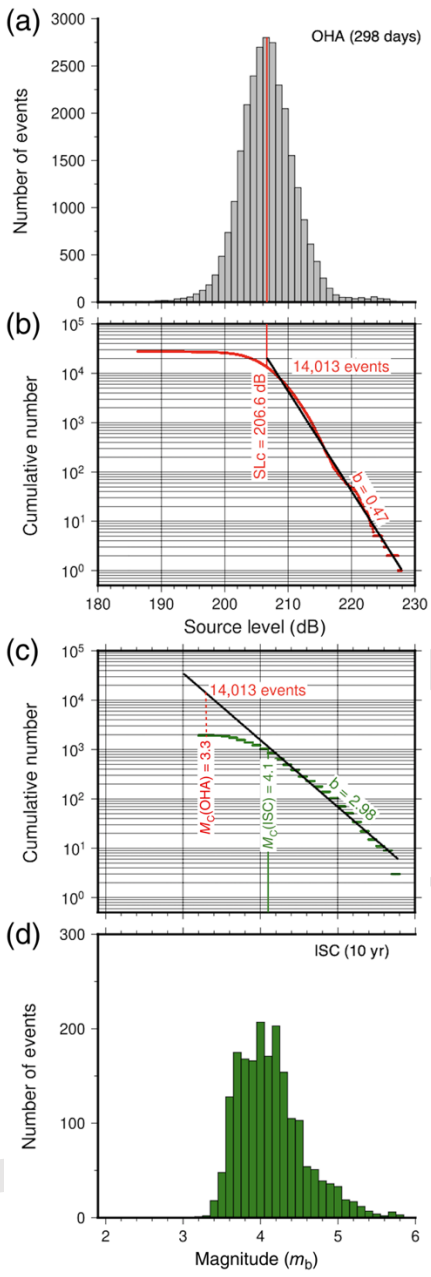

Figure 2: Completeness of source level (SL) and m_b based on best-fitting Gutenberg–Richter's laws. (a) Histogram of the hydroacoustic (OHA) catalog from June 2016 to March 2017 (298 days). (b) Cumulative number of events in the OHA catalog. The vertical line points to the completeness, SL_C 206:6 dB with a b-value of 0.47 in the SL framework. (c) Cumulative number of events in the International Seismological Centre (ISC) catalog along the Southwest Indian Ridge (SWIR) axis reported from 2010 to 2020. The vertical line points to the magnitude of completeness $M_{C(ISC)}$ = 4.1. Extrapolating the Gutenberg–Richter's law of this ISC catalog up to the number of events for which the OHA catalog is complete (14,013 events) yields to $M_{C(ISC)}$ = 3.3. (d) Magnitude histogram of the ISC events from 2010 to 2020 along the SWIR axis.

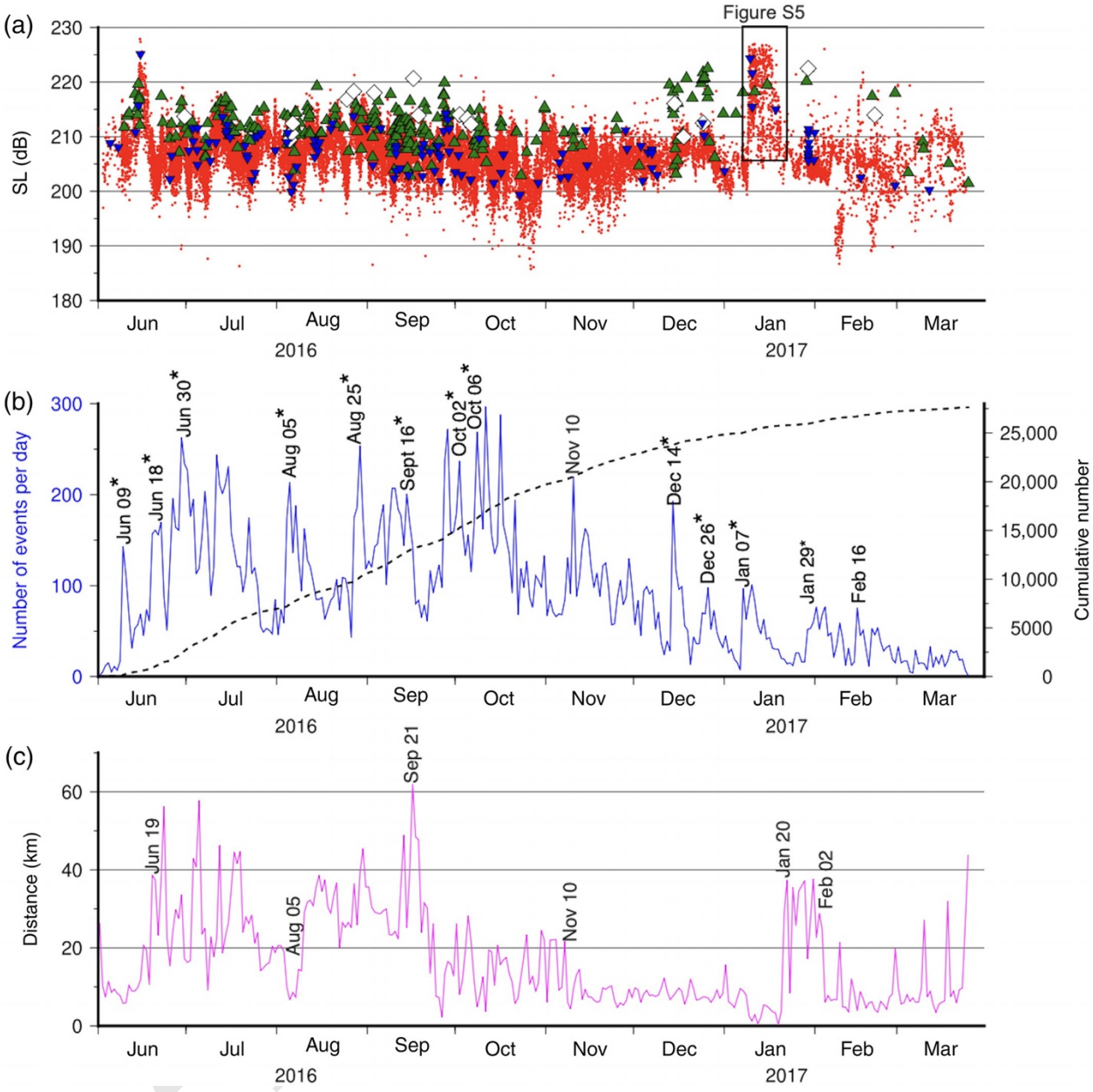

Figure 3: (a) Source level (SL) distribution of the OHA (dots), ISC (triangles), Global CMT (diamonds), and impulsive (inverted triangles) events between June 2016 and March 2017. Higher SLs between 9 and 20 January 2017 (black rectangle) are explained in Figure S5. (b) Number of events per day (solid line) and cumulative number of events versus time (dashed line). Dates mark the onset of higher seismicity between June 2016 and March 2017. Dates with asterisks point to the start of potential sequences tested against modified Omori's laws. (c) Median distance of events per day relative to a reference point (RP; marked by a cross in Fig. 1b). Dates mark significant changes in the distance of events from the RP.

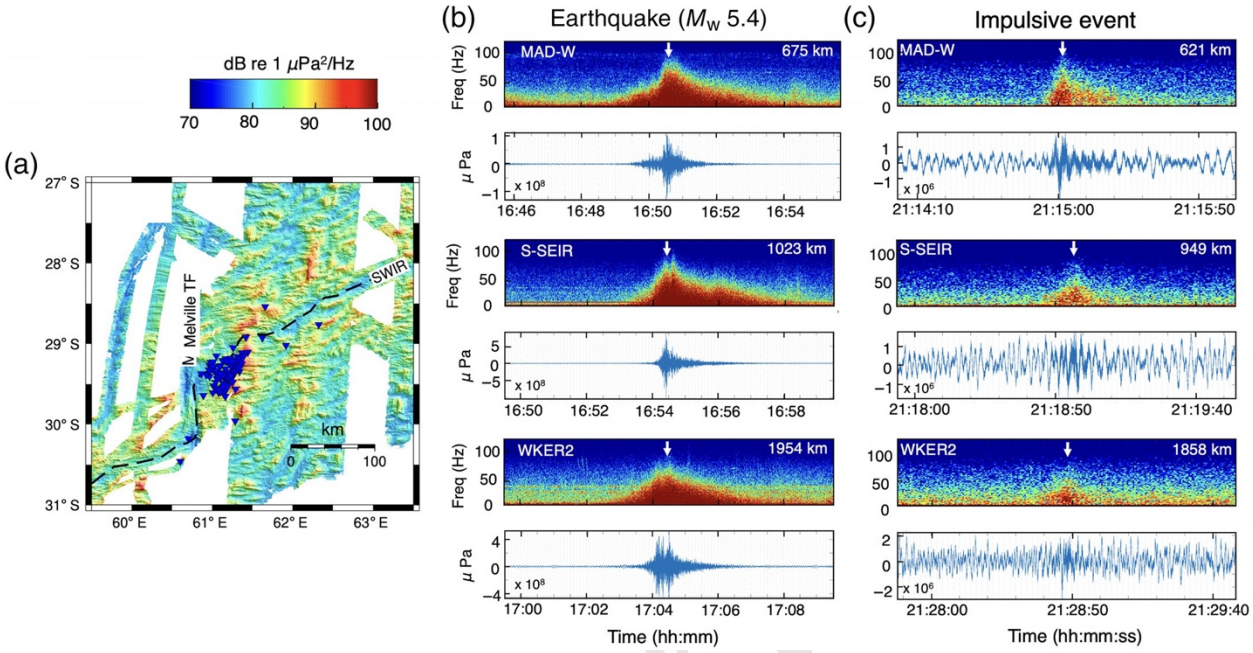

Figure 4: (a) Location of impulsive events (inverted triangles) on the slopes of bathymetric highs on the southern flank of the SWIR (dashed line) east of Melville TF. (b,c) Comparison of acoustic waveforms and spectrograms for a typical earthquake event (M_W 5.4) and for an impulsive event recorded at three sites of the OHASISBIO network (MAD-W, S-SEIR, WKER2, from top to bottom); distances in kilometers are from the earthquake location and from the cluster of impulsive events, respectively. Acoustic signals can last for ~200 s for an earthquake (T-wave) versus 10–15 s for an impulsive event (H-wave). The former stand out both in waveforms and spectrograms, whereas the latter mainly stand out in spectrograms. The white arrows point to the highest T-wave or H-wave energy arrivals.

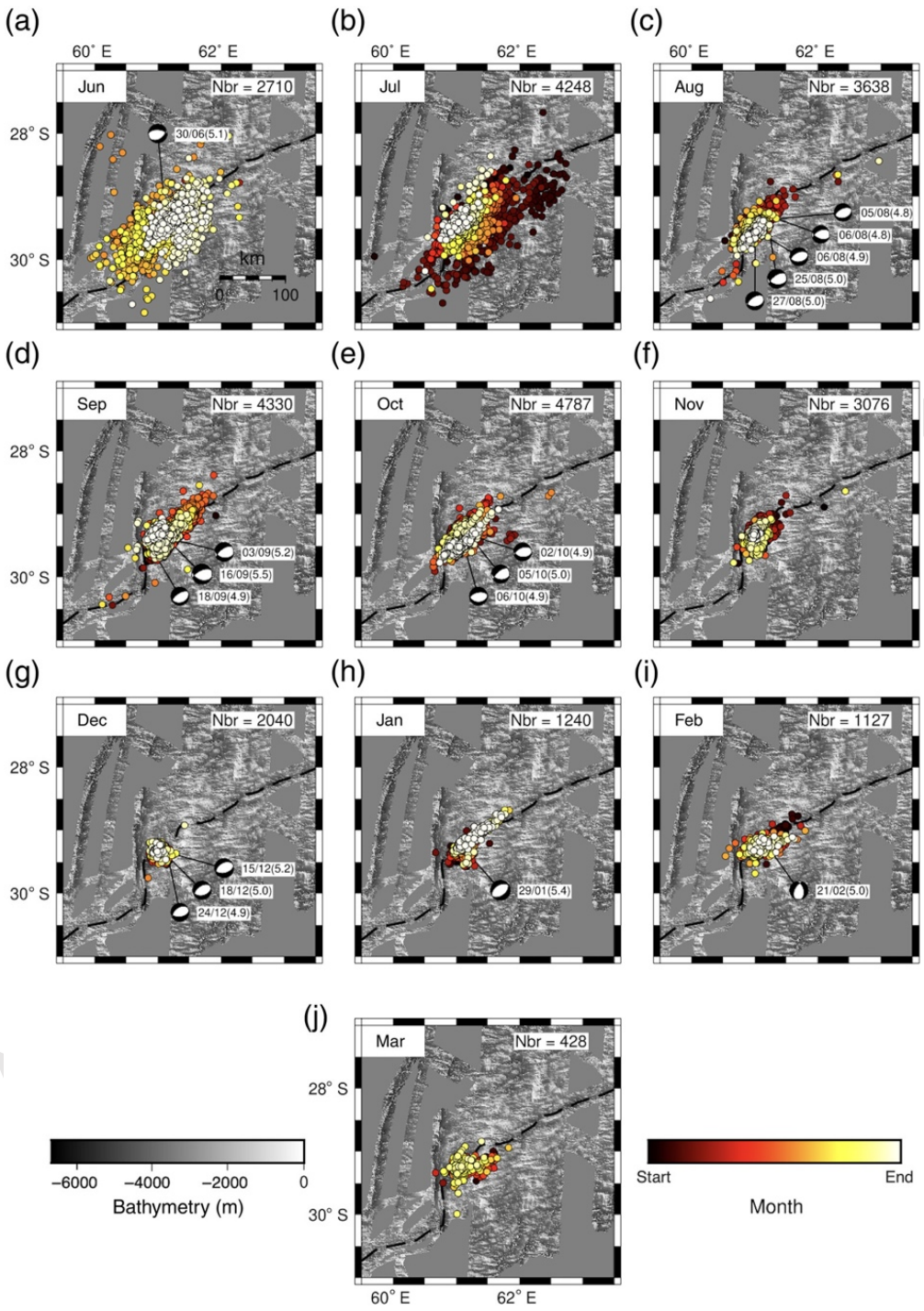

Figure 5: (a–j) Monthwise temporal distribution of events from June 2016 to March 2017, with the total number of events per month (Nbr). The dashed line shows the SWIR axis. The dark colors in the time scale denote the start of each month. Labels next to Global CMT focal mechanisms provide the date and magnitude (M_W) of the events. Note that all normal-fault planes in focal mechanisms are parallel to the SWIR axis except for the last one in February 2017 where they are parallel to the Melville transform fault (TF).

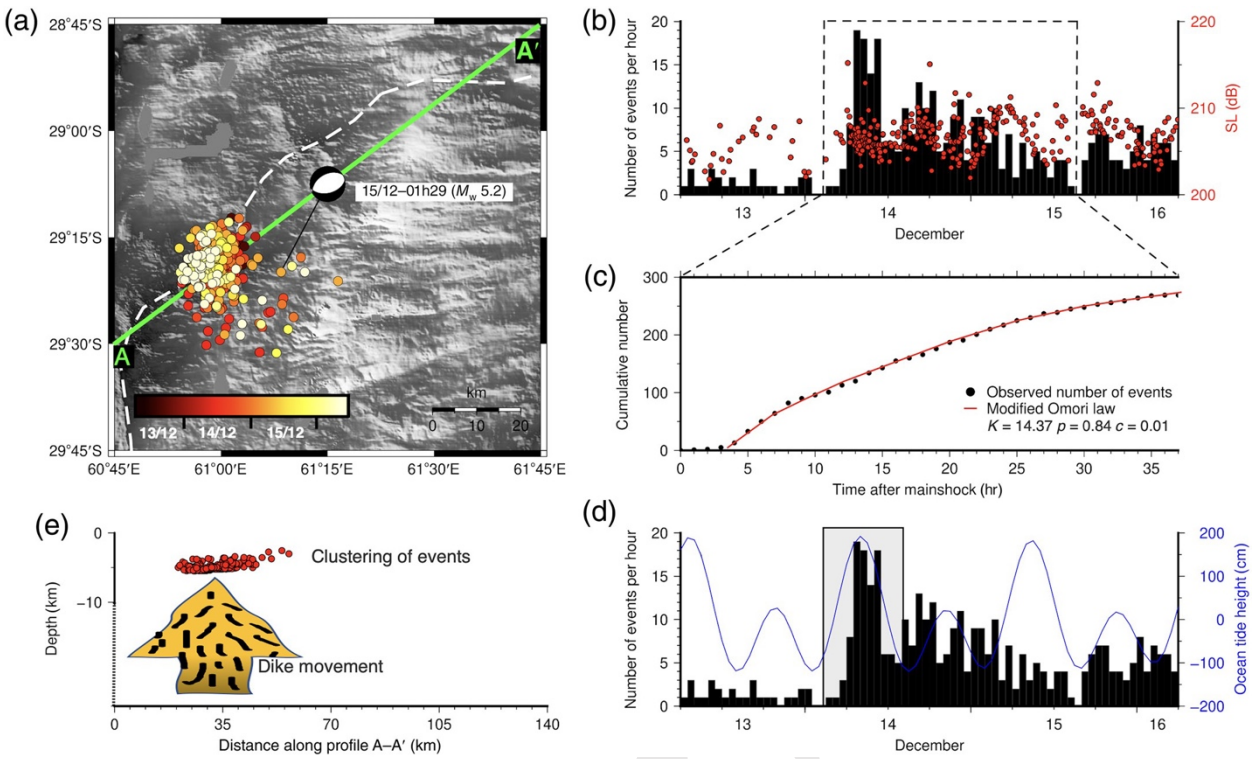

Figure 6: (a) Spatiotemporal distribution of the events between 13 December at 06:00 and 16 December at 06:00 (sequence 9), with the only Global CMT focal mechanism (15 December at 01:29, M_W 5.2) in this sequence, near its end. The dashed line shows the SWIR axis. (b) Temporal distribution of number of events per hour (histogram) with their SLs (circles). The dashed rectangle outlines the selection of events used to compute the modified Omori's law, shown in panel (c). (c) The black dots show the hourly cumulative number of events, and the solid curve shows the best-fitting modified Omori's law. (d) Temporal distribution of number of events per hour (histogram) versus ocean tide height (solid curve). This is the only sequence where high seismicity coincides with high tide (grayed area). (e) Projection of the cluster of T-wave radiating points (circles) at seafloor depth along A–A' profile (solid line in panel a). The broad vertical arrow schematizes upwelling dikes beneath the clustered events. The depth of the dikes is not constrained.

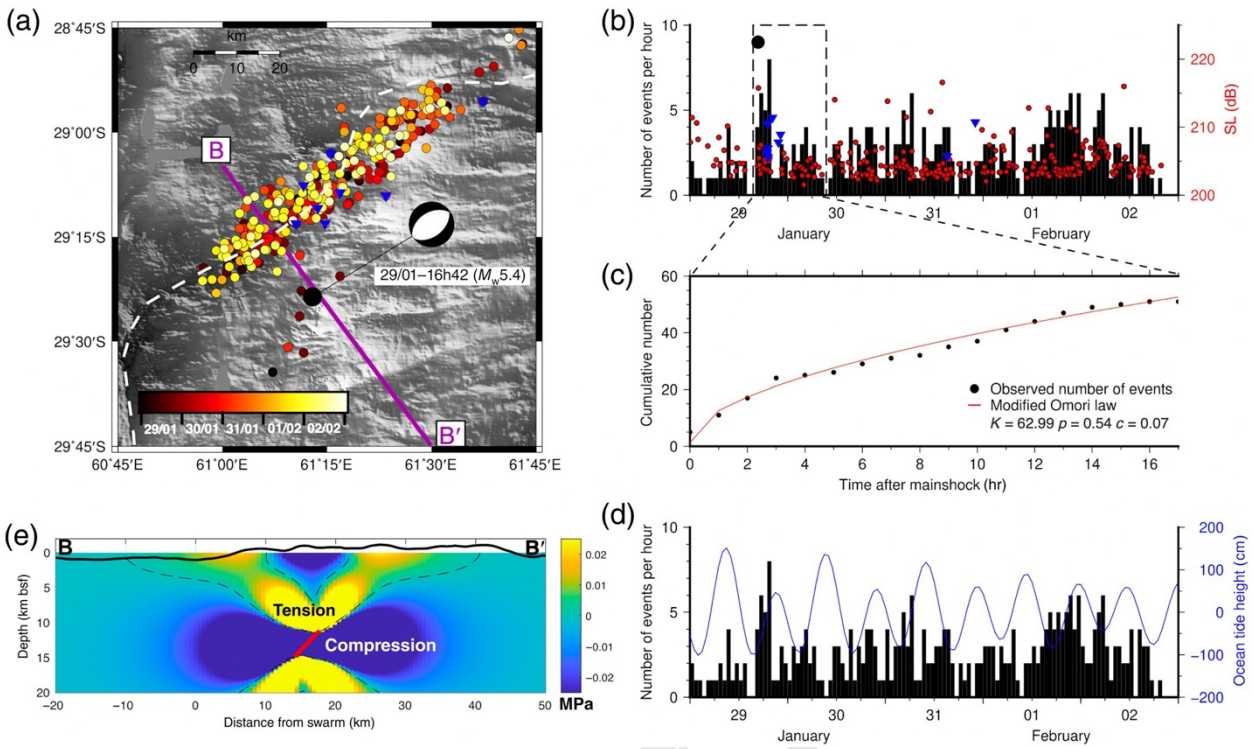

Figure 7: (a) Spatio-temporal distribution of the events between 29 January and 2 February 2017 (sequence 12) with the Global CMT focal mechanism of the strongest event that triggered the sequence on 29 January at 16:42 (M_W 5.4). The dashed line shows the SWIR axis. (b) Temporal distribution of number of events per hour (histogram) with their SLs (circles) and that of impulsive events (inverted triangles). The dashed rectangle outlines the selection of events used to compute the modified Omori's law, shown in panel (c). (c) The black dots show the hourly cumulative number of events and the solid curve shows the best-fitting modified Omori's law. (d) Temporal distribution of number of events per hour (histogram) versus ocean tide height (solid curve). (e) Schematic cross section (along B–B') showing a plausible geometry for the Global CMT fault plane (thick line), SE of the ridge axis. Contours show the predicted horizontal stress changes in MPa for an M_W 5.4 normal-slip event with a dip-slip of 18 cm over a 5.1 × 5.1 km square patch embedded in an elastic half-space with Young's modulus and Poisson's ratio 100 GPa and 0.25, respectively (Olive et al., 2016). The light colors indicate areas under tension, allowing for dike emplacements in the axial valley and/or local stress readjustments, at the origin of the observed alignment of events.

Table 1: Locations and acquisition parameters of the hydrophones of the OHASISBIO and CTBTO networks

Sites	MAD-W	MAD	MAD-E	S-SEIR	NE-AMS	SW-AMS3	WKER2	S-SWIR	H08S1	H01W1
Latitude [°S]	29.051	26.084	24.197	33.514	31.575	42.989	46.602	38.550	7.645	34.893
Longitude [°E]	54.260	58.140	63.010	70.867	83.241	74.850	60.547	52.879	72.474	114.154
Water depth [m]	1280	1260	1180	1210	2760	1160	980	1150	800	800
Sampling rate [Hz]	240	240	240	240	240	240	240	240	250	250
Sensitivity [dB]	-163.4	-163.7	-163.5	-163.5	-163.5	-168.6	-163.6	-163.3	-165.2	-165.2
Start Time	06/01/17	29/01/16	08/02/17	25/01/16	07/02/17	21/01/16	12/01/16	08/01/17	01/01/16	01/01/16
End Time	06/01/18	08/02/17	13/02/18	11/02/18	13/02/18	09/12/18	04/02/18	22/12/17	31/12/17	31/12/17
Clock drift [ppm]	-0.1004	-0.0393	-0.0466	-0.0021	-0.0466	-0.0162	-0.0080	-0.0205	N/A	N/A

Table 2: Summary of the number of events, tidal correlation, modified Omori's law parameters and interpretation of the 12 seismic sequences defined in Figure 3

Sr No	Dates	Duration (hours)	Nbr of OHA events	Impulsive events	ISC event *	GCMT event *	Tidal correlation	K #	c #	*p*-value #	Interpretation
1	09/06/16 - 10/06/16	26	136	0	N/A	N/A	NO	23.99	0.01	0.55	Magmatic swarm
2	18/06/16 - 24/06/16	144	786	0	N/A	N/A	NO	179.13	0.09	0.87	Magmatic swarm
3	30/06/16 - 02/07/16	60	515	1	*mb* = 5.2	Mw = 5.1	NO	14.47	0.09	0.88	Magmato-tectonic
4	05/08/16 - 06/08/16	30	230	2	*mb* = 4.7	Mw = 4.8	NO	198.95	0.01	0.86	Magmato-tectonic
5	25/08/16 - 26/08/16	46	130	0	*mb* = 4.5	Mw = 5.2	NO	90.95	0.07	0.58	Magmato-tectonic
6	16/09/16 - 19/09/16	55	201	0	*mb* = 5.5	Mw = 5.5	NO	9.91	0.01	0.74	Magmato-tectonic
7	02/10/16 - 04/10/16	55	357	1	*mb* = 4.8	Mw = 4.9	NO	8.16	0.07	0.95	Magmato-tectonic
8	06/10/16 - 07/10/16	24	86	0	*mb* = 4.7	Mw = 4.9	NO	10.99	0.05	0.66	Magmato-tectonic
9 $	14/12/16 - 16/12/16	37	269	0	N/A	N/A	YES	14.37	0.01	0.84	Magma upwelling
10	26/12/16 - 27/12/16	29	124	0	*mb* = 3.8	N/A	NO	18.34	0.09	0.57	Magmatic swarm
11	07/01/17 - 14/01/17	182	555	3	*mb* = 3.8	N/A	NO	91.06	0.09	0.91	Magmatic swarm
12 $	29/01/17 - 30/01/17	17	51	9	*mb* = 5.7	Mw = 5.4	NO	62.99	0.07	0.54	Extrusion after vertical dike

* N/A means there was no triggering event at the start of the sequence, otherwise its magnitude is given

Modified Omori's law parameters (equation 2)

$ Detailed description in Figures 6 and 7